

A tunable Fabry-Pérot quantum Hall interferometer in graphene

Corentin Déprez,¹ Louis Veyrat,¹ Hadrien Vignaud,¹ Goutham Nayak,¹ Kenji Watanabe,² Takashi Taniguchi,³ Frédéric Gay,¹ Hermann Sellier,¹ and Benjamin Sacépé^{1,*}

¹*Univ. Grenoble Alpes, CNRS, Grenoble INP, Institut Néel, 38000 Grenoble, France*

²*National Institute for Materials Science, 1-1 Namiki, Tsukuba 306-0044, Japan*

³*International Center for Materials Nanoarchitectonics*

Electron interferometry with quantum Hall edge channels holds promise for probing and harnessing exotic exchange statistics of non-Abelian anyons. In semiconductor heterostructures, however, quantum Hall interferometry has proven challenging and often obscured by charging effects. Here we show that high-mobility monolayer graphene equipped with a series of gate-tunable quantum point contacts that act as electron beam-splitters provides a model system to perform Fabry-Pérot quantum Hall interferometry. We observe high-visibility Aharonov-Bohm interference free of charging effects and widely tunable through electrostatic gating or magnetic field, in remarkable agreement with theory. A coherence length of $10\ \mu\text{m}$ at a temperature of $0.02\ \text{K}$ allows us to further achieve coherently-coupled double Fabry-Pérot interferometry. Our results open a new avenue for quantum Hall interferometry and the exploitation of topological excitations for quantum computation.

The wave-like behavior of electrons is exemplified in metals and semiconductors by a variety of mesoscopic phenomena stemming from quantum interference effects. Universal conductance fluctuations in coherent conductors or quantum (weak) localization due to random scattering are some vivid examples. In two dimensional electron gases, quantum interferences can be precisely tailored and harnessed using the chiral edge channels of the paradigmatic quantum Hall (QH) effect as one-dimensional, coherent electron beams. Electrostatic manipulation and partitioning of QH edge channel trajectories via local gates and quantum point contacts (QPCs) –that is, tunable beam-splitters for electrons– makes it possible to construct on-chip electronic analogues of Fabry-Pérot¹ (FP) or Mach-Zehnder² optical interferometers, usable for quantum information processing³.

Central to QH interferometry are the braiding of anyonic excitations⁴ in the fractional QH regime and the prospect of exploiting the non-Abelian properties^{5–11} of some fractional QH states¹² for topological quantum computation¹³. Winding fractional edge excitations around localized bulk ones is the elementary process sensitive to the anyonic statistical exchange phase⁴ –a quantity evidenced via shot-noise measurements¹⁴. Such a braiding process of anyonic excitations has been demonstrated very recently in Fabry-Pérot interferometers¹⁵ in which an edge channel, partially reflected between two QPCs, encloses localized excitations into an interfering loop and picks up the anyonic statistical phase. Moreover, advanced devices based on coherently-coupled double Fabry-Pérot interferometers have been envisioned as a possible route for achieving topologically protected qubits addressable via braiding operations⁶.

The body of work on QH Fabry-Pérot interferometers performed in GaAs heterostructures^{16–24} has, however, faced various difficulties. Observing quantum interference tunable by gate electrodes and magnetic field through the Aharonov-Bohm effect has proven often

disguised by charging effects in the Fabry-Pérot cavity^{16–20,23,25}. The Coulomb blockade^{26–28} that is due to the small interferometer sizes has long hindered progress and demands device architectures that implement various types of screening electrodes to mitigate charging effects^{15,22,24}. Furthermore, the delicate edge channel reconstructions in GaAs involving neutral modes or counter-propagating charge modes²⁹ can complicate interferometry³⁰. All these highlight the need for exploring QH interferometry in other two-dimensional electron gases.

Here, we demonstrate that graphene monolayer is a promising alternative platform for QH Fabry-Pérot interferometry, free of charging effects, thereby opening a new pathway for anyon interferometry^{15,24}. Graphene comes forth as an ideal two-dimensional electron gas with all necessary features: high-mobility³¹, fractional quantum Hall effect^{32,33} with large energy gaps³⁴, including possible non-Abelian states^{35,36}, helical edge channels at charge neutrality^{37,38}, gate-tunability, and versatility of van der Waals heterostructures³⁹. Similarly for the graphene bilayer^{40–42}.

Yet, gate tunable QPCs –the key component to construct elaborated QH interferometers (see Fig. 1)– has proven challenging to realize due to the gapless band structure of graphene. Depleting the electron gas through electrostatic gating accumulates holes and yields conducting pn-junctions⁴³ that short-circuit QPC constrictions⁴⁴. Other alternatives involve partitioning at a pn junctions^{45,46}, or etched constrictions⁴⁷ that yield devices subject to charging effects. We remedy this with the use of high-mobility graphene in the QH regime for which an insulating, broken-symmetry state develops and opens an energy gap at the charge neutrality point separating the conduction band from the valence band³⁷. This gap is essential for the functioning of split gates as full-fledged QPC with tunable edge channel transmission⁴⁸: It suppresses some possible charge transfers at the pn junction

surrounding the split-gates (see drawing in Fig. 2d).

We thus devised our device on the basis of a high-mobility graphene van der Waals heterostructure made with an hexagonal boron nitride (hBN)-encapsulated graphene monolayer³¹ resting atop a graphite flake that acts as a back-gate electrode. As depicted in Fig. 1a, three pairs of split-gates of 20 nm gap, on top of the heterostructure, serve as QPCs and define a double FP cavity. Plunger gates located on the edges of each cavity are used to move the trajectory of the interfering QH edge channel and modulate the effective interferometer areas. The device we focus on in this report is shown in Fig. 1b with QPCs highlighted in red and labeled QPC₁, QPC₂ and QPC₃, plunger gates in orange and ohmic contacts in yellow (see Supp. Section III for the design characteristics of the QPC geometry). This triple QPC configuration enables us to operate three FP interferometers that we denote small (QPC₂-QPC₃), medium (QPC₁-QPC₂) and large (QPC₁-QPC₃) interferometers, whose geometrical areas are 3.1, 10.7 and 13.1 μm^2 , respectively (see Supp. Table S2).

To operate the QH-FP interferometers, the graphene electron gas is subjected to a perpendicular magnetic field, B , to reach the quantum Hall regime. Prior to electron interferometry, each QPC transmission is individually characterized by mapping out the diagonal resistance R_D measured across contacts V_D^+ and V_D^- as a function of back-gate and split-gate voltages (see Supp. Fig. S5). We choose to work at bulk filling fractions $\nu_b = n_b\phi_0/B$ (n_b is the bulk charge carrier density, $\phi_0 = h/e$ is the flux quantum with h the Planck constant and e the electron charge) such that two electron-type edge channels of the zeroth Landau level propagate on the graphene edges, as indicated by a Hall conductance of $2e^2/h$ (see Supp. Fig. S7). A proper tuning of the split-gate voltages enables us to partially transmit either the inner or outer edge channel at the QPCs. Other configurations with only one electron-type edge channel present in the bulk have also been studied (see Supp. Section XIII).

Widely tunable quantum interference

The quantum interferences in the small electronic Fabry-Pérot interferometer readily show up in Fig. 2a-c, which display the oscillatory behavior of the diagonal resistance R_D as a function of the plunger-gate voltage $V_{\text{pg}2}$. For this measurement performed at $B = 14$ T, the QH-FP interferometer operates at $\nu_b = 1.5$. We tuned QPC₂ and QPC₃ to a transmission of the outer edge channel $T_2 = 0.60$ and $T_3 = 0.47$, respectively, leaving the inner one fully backscattered and localized in the FP cavity (see Supp. Fig. S6 for the QPCs transmission curves). In this configuration, R_D oscillates with about 50% visibility (see Fig. 2a and b) over nearly the whole voltage range spanned by the plunger gate (Fig. 2c), starting around $V_{\text{pg}2} = -0.3$ V down to $V_{\text{pg}2} = -4$ V. Further oscillations extending to positive $V_{\text{pg}2}$ values when electrons are accumulated beneath the

plunger gate are shown in Supp. Fig. S8. These results showing more than 280 resistance oscillations demonstrate the high stability and wide tunability of our interferometer.

The oscillatory behavior of the diagonal resistance upon depleting the electron gas beneath the plunger gate is a direct consequence of the modulation δA of the interferometer area defined by the interfering edge channel. Changing the flux through the interferometer via δA yields a variation $\delta\varphi = 2\pi B\delta A/\phi_0$ of the Aharonov-Bohm phase picked up by the electrons. The flux-modulated succession of constructive and destructive electron wave-function interferences is thus reflected in the stark oscillations of the diagonal resistance.

Plunger-gate electrostatics

Inspecting the oscillations more closely on a smaller span around two different plunger-gate voltages, $V_{\text{pg}2} = -3$ V and -1 V in Fig. 2a and b, respectively, we see that the period depends upon the plunger-gate voltage. This behavior can be tracked by computing the Fourier transform restricted to a small voltage window sliding over the entire $V_{\text{pg}2}$ range. The resulting Fourier amplitude shown in Fig. 2e as a function of $V_{\text{pg}2}$ and plunger-gate-voltage frequency $f_{\text{pg}2}$ displays a single peak that disperses to lower frequency upon decreasing $V_{\text{pg}2}$ to more negative values. This is consistent with the larger periodicity observed in Fig. 2a with respect to that of Fig. 2b. Notice that a second harmonic indicated by the black arrow in the inset of Fig. 2e is also visible, mostly at large negative $V_{\text{pg}2}$.

The $V_{\text{pg}2}$ -dispersion of the oscillations frequency reflects the electrostatics of the plunger gate. Depleting the graphene electron gas and then accumulating hole states locally under the plunger gate repels the interfering edge channel towards the interior of the QH-FP interferometer as illustrated in the schematics in Fig. 2d, therefore reducing the effective area. The abrupt drop of the oscillation frequency $f_{\text{pg}2}$ at $V_{\text{pg}2} \simeq -0.3$ V corresponds to the expulsion out of the area beneath the plunger gate of the interfering edge channel that was initially propagating along the graphene edge. This expulsion occurs when the graphene beneath the plunger gate reaches charge neutrality (or filling fraction 1 for the inner edge channel interfering case, see Fig. 2d). Notice that near this regime, the apparent reduction of the oscillation amplitude is not physical but results from a too fast oscillation frequency with respect to the bandwidth of our measurement and the constant sweep rate of the plunger gate voltage. For more negative $V_{\text{pg}2}$, $f_{\text{pg}2}$ decreases more slowly due to the accumulation of holes and the ensuing displacement of the pn-junction further away from the plunger gate.

The plunger gate tuning of the magnetic flux is demonstrated by the magnetic field dependence of the oscillations period. The area variation $\Delta A = \phi_0/B$ that yields a change of one flux quantum in the interferometer relates to the plunger-gate voltage period $\Delta V_{\text{pg}2}$

by $\Delta A = \alpha \Delta V_{\text{pg}2}$, where α is the (non-linear) lever arm of the gate. As $f_{\text{pg}2} = 1/\Delta V_{\text{pg}2}$, the quantity $f_{\text{pg}2}/B = \alpha/\phi_0$ depends only on the electrostatic displacement of the pn interface that is encoded in α . Fig. 2f displays $f_{\text{pg}2}/B$ as a function of $\bar{V}_{\text{pg}2}$, gathered from Fig. 2e and from similar data obtained at $B = 11$ and 8 T, and also by making interfering the inner edge channel through a suitable tuning of the QPCs (see Supp. Fig. S9). Here, $\bar{V}_{\text{pg}2}$ is the plunger-gate voltage shifted with respect to the voltage that expels the inner or outer edge channel. Despite a large variation of magnetic field, and hence of oscillations periods, all data collapse onto the same curve, confirming the flux periodicity.

Furthermore, this data collapse draws the $\bar{V}_{\text{pg}2}$ -evolution of the lever arm, which can be directly compared to numerical simulations of the electrostatic displacement of the pn junction in our device geometry (see Supp. Fig. S10). The resulting computation of α/ϕ_0 shown by the black line in Fig. 2f consistently fits the data and therefore demonstrates the ϕ_0 -periodicity of the oscillations, bearing out the Aharonov-Bohm origin of the resistance oscillations.

Aharonov-Bohm effect vs Coulomb blockade

A critical aspect of QH-FP interferometers lies in the possibility that the resistance oscillations result from charging effects in the FP cavity^{26–28}, instead of Aharonov-Bohm quantum interference. Thorough studies on this issue showed that these two competing phenomena can be straightforwardly differentiated by the magnetic-field dependence of the gate-induced oscillations^{17,19,23,27,28}: For the Aharonov-Bohm effect, resistance oscillations in the B - V_{pg} plane shall draw diagonal lines of negative slope, indicating constant flux $\phi = B\delta A + A\delta B$ through the interferometer, whereas a zero or positive slope is expected for the Coulomb blockade effect. This led us to perform systematic measurements of the resistance oscillations as a function of plunger-gate voltage and magnetic-field variation δB . Figure 3 displays two typical resistance maps obtained with the small interferometer (Fig. 3a) and with the large one (Fig. 3b), both at $B = 14$ T with the outer edge channel interfering. For both cases, resistance maxima (minima) draw lines of negative slope: Upon increasing magnetic field the lines go to more negative values of V_{pg} , hence shrinking the area to maintain the Aharonov-Bohm phase (flux) constant. This behavior that we constantly observed in all configurations, regardless of the interferometer size, magnetic field value, bulk filling factor being 1 or 2, or which edge channel is interfering (see Supp. Sections X and XI), definitely rules out the alternative Coulomb blockade scenario.

The absence of Coulomb blockade even in the smaller interferometer, whose dimensions are similar to those in GaAs devices that exhibit Coulomb blockade¹⁷, points to a specificity of the hBN-graphene heterostructure. For our devices, the main source of charging effect mitigation is the close proximity of the graphite back gate elec-

trode. Following the theoretical approach of Ref.²⁷, we evaluated the various capacitances involved in our devices and calculated the parameter $\xi = \frac{C_{\text{eb}}}{C_{\text{b}} + C_{\text{eb}}}$ with C_{b} the bulk-to-gate capacitance and C_{eb} the edge-to-bulk capacitance, which defines the Aharonov-Bohm ($\xi \ll 1$) or Coulomb-dominated ($\xi \sim 1$) operating regime²⁷ (see Supp. Section XIV). For the smallest interferometer, we obtain a charging energy of $18 \mu\text{eV}$ similar to that of GaAs devices of similar sizes operating in the Aharonov-Bohm regime²⁴, and $\xi \simeq 6 \times 10^{-3}$, which is fully consistent with the absence of Coulomb blockade in our graphene devices. Yet, we also observed Aharonov-Bohm interference in two other graphene devices equipped instead with a 285 nm thick SiO_2 back-gate dielectric (see Supp. Section XIII). Despite a reduction of about 15 of the back-gate surface capacitance, we estimate $\xi \simeq 7 \times 10^{-2}$ which remains consistent with the Aharonov-Bohm regime. The systematic presence of back-gate electrodes, and to a lesser extent, the close proximity of the top-gate electrodes in hBN-encapsulated graphene therefore provide efficient screening of charging effects that enables to observe Aharonov-Bohm interference.

The magnetic-field period ΔB of the Aharonov-Bohm oscillations provides a direct measure of the effective area A_{AB} drawn by the interfering edge channel. For the three interferometers we obtained $\Delta B = 1.32, 0.40$ and 0.27 mT corresponding to $A_{\text{AB}} = 3.1, 10.4$ and $15.0 \mu\text{m}^2$, which is consistent with our expected geometrical areas of $3.1 \pm 0.4, 10.7 \pm 1.2$ and $13.1 \pm 1.8 \mu\text{m}^2$, substantiating the ϕ_0 -periodicity obtained with the electrostatic analysis of the plunger-gate effect. Notice that the precision of the geometrical areas is limited by the uncertainty in the optical determination of the graphene physical edges position, which could easily explain the small differences with the measured Aharonov-Bohm areas.

Decoherence and thermal broadening

The loss of visibility in QH interferometers is a fundamental question that encompasses several phenomena such as thermal broadening or quantum decoherence by inelastic processes and energy relaxation. We investigated the coherence properties of our interferometers through the joint analysis of the bias and temperature dependence of the visibility. The multiple QPCs configuration enables us to systematically study the coherence properties for three different cavity lengths. We begin with the out-of-equilibrium measurements performed with a dc voltage bias V_{dc} applied on the source contact (the drain contact is kept grounded). Electrons injected at a finite energy $\delta\epsilon$ above the Fermi energy of the cavity have a phase shift $2\pi\delta\epsilon 2L/hv$ proportional to twice the length L of the edge channel between the two QPCs and to the edge-excitation velocity v . This additional phase shift that adds up to the Aharonov-Bohm phase can yield theoretically a variety of oscillation patterns as a function of magnetic flux and voltage bias, which depend on the voltage drop across the device (see Supp. Section

XV). For a symmetric drop at the two QPCs ($V_{\text{dc}}/2$ and $-V_{\text{dc}}/2$ on the source and drain), the resistance oscillations draw a checkerboard pattern of the form $\delta R_{\text{D}} \propto \cos(2\pi\phi/\phi_0)\cos(2\pi eV_{\text{dc}}/E_{\text{Th}})$. For a fully asymmetric drop (V_{dc} and 0 on the source and drain) a diagonal strip pattern of the form $\delta R_{\text{D}} \propto \cos(2\pi\phi/\phi_0 - 4\pi eV_{\text{dc}}/E_{\text{Th}})$ is expected instead. In these expressions, the oscillations period as a function of V_{dc} is governed by the ballistic Thouless energy $E_{\text{Th}} = h/\tau$ related to the traveling time $\tau = L/v$ between the two QPCs^{4,28}.

For the large interferometer at $B = 14$ T, the resistance oscillations at finite bias (Fig. 3d) draw a checkerboard pattern similar to those observed in GaAs devices^{18,24,49}. The resulting oscillations decay quickly as a function of the dc voltage V_{D}^{dc} (measured across the diagonal contacts V_{D}^+ and V_{D}^-), indicating that some energy relaxation processes are at play at finite bias (see Supp. Fig. S18). Repeating the measurements on the two other interferometers yields similar patterns (see Supp. Section XV), though with a notable difference in the form of the checkerboard which tends to be tilted towards a diagonal strip pattern upon reducing the interferometer size, as illustrated in Fig. 3c for the small interferometer. This tilt can be accounted for by an incomplete equilibration of chemical potential carried by the electron flow, which partially maintains the asymmetric voltage drop across the cavity. Calculation of the theoretical FP transmission with an unbalanced voltage drop describes very well the observed tilted checkerboard, as shown in Fig. 3e and f (theoretical analysis and additional data are provided in Supp. Section XV).

The key parameter extracted from these checkerboards is the Thouless energy of the cavity $E_{\text{Th}} = hv/L$ that is given by the V_{D}^{dc} -periodicity. The resulting values shown in Fig. 3i for the three interferometers are found to consistently scale with $1/L$.

Besides, theory predicts that the temperature dependence of the oscillations visibility also relates to the Thouless energy⁴. The blurring of interference by the thermal broadening of the impinging electrons leads to an exponential suppression of the visibility with temperature, which follows $\exp(-4\pi^2 k_{\text{B}}T/E_{\text{Th}})$ with k_{B} the Boltzmann constant. In Fig. 3g and h we show the T -dependence of the resistance oscillations for the three interferometers. A clear exponential suppression of the visibilities is obtained in all cases, which is fitted with $\exp(-T/T_0)$ (dashed lines in Fig. 3h). The resulting $4\pi^2 k_{\text{B}}T_0$ values that we append to Fig. 3i conspicuously scale as $1/L$ and are furthermore in excellent agreement with the Thouless energies extracted from the checkerboard patterns, bearing out a visibility limited mainly by thermal broadening. The slope in Fig. 3i further enables us to extract an estimate of the edge velocity $v = 1.4 \times 10^5$ m.s⁻¹, which is of the same order as that obtained in GaAs devices^{18,24,50}, though here at a much higher magnetic field. Finally, a phase coherence length of $10 \mu\text{m}$ at our base temperature can be assessed from the exponential suppression of the

visibility with the perimeter of the interferometer, after corrections accounting for thermal broadening (see Fig. S19). This global set of data that complies with most of the theoretical expectations⁴ therefore demonstrates graphene to be a highly tunable, model platform for QH-FP interferometry.

Coherently-coupled double FP interferometer

Here we operate our device in a three QPCs configuration to show that the large FP interferometer remains coherent upon turning on backscattering at the middle QPC. As sketched in Fig. 4a and b, Aharonov-Bohm interference depends upon three fluxes, $\phi_{1,2,3}$, defined by the three cavity areas (blue, green and yellow in Fig. 4b, respectively). Each of them can be tuned by the magnetic field and one or two plunger gates. Figure 4c displays the resistance of the device for the three QPCs tuned at partial transmission of the outer edge channel, with a total transmission $T \simeq 0.46$, upon varying both plunger-gate voltages V_{pg1} and V_{pg2} . The resistance oscillates with both gate voltages and draws a regular pattern characteristic of the flux variation ϕ_1 with V_{pg1} (blue FP cavity), and ϕ_2 with V_{pg2} (green FP cavity). Coherence through the double interferometer is unveiled in the 2D Fourier transform in Fig. 4e. In addition to the two peaks at frequencies $(f_{\text{pg1}}, f_{\text{pg2}}) = (53 \text{ V}^{-1}, 0 \text{ V}^{-1})$ and $(0 \text{ V}^{-1}, 60 \text{ V}^{-1})$ corresponding to fluxes ϕ_1 and ϕ_2 respectively, a third peak emerges at $(f_{\text{pg1}}, f_{\text{pg2}}) = (53 \text{ V}^{-1}, 60 \text{ V}^{-1})$, indicative of a joint modulation by both plunger gates and hence a modulation of the double cavity flux ϕ_3 . Inspection of the four quadrants of the Fourier transform in Fig. S21 shows that a fourth peak related to a $\phi_1 - \phi_2$ contribution is present but with a lower amplitude than the ϕ_3 contribution. This indicates that the ϕ_3 peak is mainly the result of the interference process for which electron wavefunctions interfere coherently after passing twice (back and forth) through the partially-transmitting middle QPC. (see Supp. Section XVIII for a detailed theoretical analysis)

Figure 4d shows a complementary measurement where the magnetic field is varied together with the plunger-gate voltage V_{pg2} acting on the area of the small interferometer. We observe diagonal stripes similar to those in Fig. 3a and characteristic of the Aharonov-Bohm effect for the small cavity with flux ϕ_2 (see peak at $(f_{\text{B}}, f_{\text{pg2}}) = (0.79 \text{ mT}^{-1}, 90 \text{ V}^{-1})$ in Fig. 4f), but with an additional wiggling. This wiggling results from the Aharonov-Bohm oscillations of the medium interferometer (in series with the small one) via the flux ϕ_1 , which is independent of V_{pg2} and corresponds to the peak at $(f_{\text{B}}, f_{\text{pg2}}) = (2.54 \text{ mT}^{-1}, 0 \text{ V}^{-1})$ in the Fourier transform (see Fig. 4f). The double cavity flux ϕ_3 , which depends upon both B and V_{pg2} , leads to a peak at $(f_{\text{B}}, f_{\text{pg2}}) = (3.49 \text{ mT}^{-1}, 90 \text{ V}^{-1})$ with a magnetic field periodicity which corresponds to the double cavity area, that is, the sum of the small and medium cavity areas. The precise shape of the wiggling of the diagonal stripes is

a direct evidence of the contribution of the double cavity flux (see Supp. Section XVIII for an additional measurement configuration).

The observation of the flux periodicity ϕ_3 , together with a careful Fourier analysis in the four quadrants (see Supp. Section XVIII), provides compelling evidence that electron interference occurs through the central QPC at partial transmission, and hence that both FP cavities are coherently coupled. Such a tunable multiple FP interferometer paves the way to more advanced devices in which sequential transfer of single particles at the central QPC, controlled for instance with an anti-dot in the QPC constriction, would enable braiding schemes for non-Abelian anyons⁶.

Conclusion and outlook

Finally, the high-visibility Aharonov-Bohm interference that we observe with remarkable agreement with the non-interacting theory⁴ demonstrates the relevance of graphene for performing prototypical QH-FP interferometry with integer quantum Hall edge channels. The high mobility and the versatility of the graphene van der Waals heterostructures turn out to be pivotal to harness fine control of QH edge-channel transmissions in QPCs⁴⁸, and therefore construct advanced gate-tunable interferometers. With further study in the fractional quantum Hall regime, this graphene platform gives new opportunities for anyon physics in QH interferometers, potentially extendable to time-resolved electron quantum optics experiments³. Besides, the recent advances in coupling graphene QH edge channels with superconductivity^{51–53} may lead to a variety of novel interferometry devices⁵⁴ in which proximity-induced topological superconductivity could be intertwined with QH interferometry for read-out or braiding schemes. Such perspectives could in turn open alternative pathways for quantum-information processing of topological excitations^{55–57}.

Note: A very recent work (<https://arxiv.org/abs/2008.12285>) that appeared during the reviewing of our manuscript confirmed our conclusions with similar graphene devices.

METHODS

Sample fabrication

hBN/graphene/hBN heterostructures were assembled from exfoliated flakes using the van der Waals pick-up technique³¹. The substrates are highly doped Si wafers with a 285 nm thick SiO₂ layer. For the sample discussed in the main text (BNGr74), the heterostructure is deposited on a thin layer of graphite that serves as a back-gate electrode. Contacts were patterned by electron-beam lithography and metalized by e-gun evaporation of a Cr/Au bilayer after etching of the stack with a CHF₃/O₂ plasma directly through the resist pattern used to define the contacts. The electrostatic plunger and

split gates were obtained with a second electron-beam lithography step and subsequent evaporation of Pd. The graphite layer for sample BNGr74 was also contacted at this step on a purposely uncovered part. Two other samples (BNGr64 and BNGr30) discussed in Supp. Section XIII were prepared without graphite-gate electrode but with the hBN/graphene/hBN heterostructure resting directly atop the Si/SiO₂ substrate.

Measurements

Measurements were performed in a dilution fridge reaching a base temperature of 0.01 K and equipped with a superconducting solenoid. To ensure good electron thermalization, the fridge is equipped with room-temperature feedthrough filters, highly-dissipative wiring, copper-powder filters at the mixing chamber stage, and cryogenic-compatible capacitors to ground on each line mounted directly on the sample holder. Devices were measured in four-terminal, voltage-bias configuration using an ac voltage of 5 μ V and low-frequency lock-in amplifier techniques. Current was measured with a home-made current-voltage converter. Non-linear transport measurements were carried out by adding a dc voltage between source and drain contacts and measuring the dc and ac components of the diagonal voltage V_D . Measurements of the resistance oscillations as a function of magnetic field and plunger-gate voltage were performed by using the current decay of the superconducting solenoid in persistent mode while sweeping the plunger-gate voltage with a 20 bits home-made voltage source. All room-temperature low-noise pre-amplifiers were thermalized in a home-made, temperature-controlled box to get rid of thermal drifts of input voltage offsets.

DATA AVAILABILITY

The data that support the findings of this study are available from the corresponding author upon reasonable request.

ACKNOWLEDGMENTS

We thank I. Aleiner for valuable discussions. We thank S. Dumont for the development of dedicated low-noise, high stability voltage sources and F. Blondelle for his technical support. Samples were prepared at the Nanofab facility of Néel Institute. This work was supported by the H2020 ERC grant *QUEST* No. 637815. K.W. and T.T. acknowledge support from the Elemental Strategy Initiative conducted by the MEXT, Japan, Grant Number JPMXP0112101001, JSPS KAKENHI Grant Number JP20H00354 and the CREST(JPMJCR15F3), JST.

- * Corresponding author : benjamin.sacepe@neel.cnrs.fr
- ¹ van Wees, B. J. *et al.* Observation of zero-dimensional states in a one-dimensional electron interferometer. *Phys. Rev. Lett.* **62**, 2523–2526 (1989).
 - ² Ji, Y. *et al.* An electronic mach-zehnder interferometer. *Nature* **422**, 415–418 (2003).
 - ³ Bäuerle, C. *et al.* Coherent control of single electrons: a review of current progress. *Reports on Progress in Physics* **81**, 056503 (2018).
 - ⁴ Chamon, C., Freed, D. E., Kivelson, S. A., Sondhi, S. L. & Wen, X. G. Two point-contact interferometer for quantum Hall systems. *Phys. Rev. B* **55**, 2331–2343 (1997).
 - ⁵ Fradkin, E., Nayak, C., Tsvetlik, A. & Wilczek, F. A Chern-Simons effective field theory for the Pfaffian quantum Hall state. *Nuclear Physics B* **516**, 704 – 718 (1998).
 - ⁶ Das Sarma, S., Freedman, M. & Nayak, C. Topologically Protected Qubits from a Possible Non-Abelian Fractional Quantum Hall State. *Phys. Rev. Lett.* **94**, 166802 (2005).
 - ⁷ Bonderson, P., Kitaev, A. & Shtengel, K. Detecting Non-Abelian Statistics in the $\nu = 5/2$ Fractional Quantum Hall State. *Phys. Rev. Lett.* **96**, 016803 (2006).
 - ⁸ Chung, S. B. & Stone, M. Proposal for reading out anyon qubits in non-Abelian $\nu = 12/5$ quantum Hall state. *Phys. Rev. B* **73**, 245311 (2006).
 - ⁹ Stern, A. & Halperin, B. I. Proposed Experiments to Probe the Non-Abelian $\nu = 5/2$ Quantum Hall State. *Phys. Rev. Lett.* **96**, 016802 (2006).
 - ¹⁰ Feldman, D. E. & Kitaev, A. Detecting non-abelian statistics with an electronic mach-zehnder interferometer. *Phys. Rev. Lett.* **97**, 186803 (2006).
 - ¹¹ Stern, A., Rosenow, B., Ilan, R. & Halperin, B. I. Interference, Coulomb blockade, and the identification of non-Abelian quantum Hall states. *Phys. Rev. B* **82**, 085321 (2010).
 - ¹² Banerjee, M. *et al.* Observation of half-integer thermal Hall conductance. *Nature* **559**, 205–210 (2018).
 - ¹³ Nayak, C., Simon, S., Stern, A., Freedman, M. & Das Sarma, S. Non-Abelian anyons and topological quantum computation. *Rev. Mod. Phys.* **80**, 1083–1159 (2008).
 - ¹⁴ Bartolomei, H. *et al.* Fractional statistics in anyon collisions. *Science* **368**, 173–177 (2020).
 - ¹⁵ Nakamura, J., Liang, S., Gardner, G. C. & Manfra, M. J. Direct observation of anyonic braiding statistics. *Nature Physics* **16**, 931–936 (2020).
 - ¹⁶ Camino, F. E., Zhou, W. & Goldman, V. J. $e/3$ Laughlin quasiparticle primary-filling $\nu = 1/3$ interferometer. *Phys. Rev. Lett.* **98**, 076805 (2007).
 - ¹⁷ Zhang, Y. *et al.* Distinct signatures for Coulomb blockade and Aharonov-Bohm interference in electronic Fabry-Perot interferometers. *Phys. Rev. B* **79**, 241304 (2009).
 - ¹⁸ McClure, D. T. *et al.* Edge-state velocity and coherence in a quantum Hall Fabry-Pérot interferometer. *Phys. Rev. Lett.* **103**, 206806 (2009).
 - ¹⁹ Ofek, N. *et al.* Role of interactions in an electronic Fabry-Perot interferometer operating in the quantum Hall effect regime. *PNAS* **107**, 5276–5281 (2010).
 - ²⁰ McClure, D. T., Chang, W., Marcus, C. M., Pfeiffer, L. N. & West, K. W. Fabry-Perot Interferometry with Fractional Charges. *Phys. Rev. Lett.* **108**, 256804 (2009).
 - ²¹ Willett, R. L., Nayak, C., Shtengel, K., Pfeiffer, L. N. & West, K. W. Magnetic-Field-Tuned Aharonov-Bohm Oscillations and Evidence for Non-Abelian Anyons at $\nu = 5/2$. *Phys. Rev. Lett.* **111**, 186401 (2013).
 - ²² Choi, H. K. *et al.* Robust electron pairing in the integer quantum hall effect regime. *Nature Commun.* **6**, 7435 (2015).
 - ²³ Sivan, I. *et al.* Observation of interaction-induced modulations of a quantum Hall liquid’s area. *Nature Commun.* **7**, 12184 (2016).
 - ²⁴ Nakamura, J. *et al.* Aharonov-Bohm interference of fractional quantum Hall edge modes. *Nature Physics* **15**, 563–569 (2019).
 - ²⁵ Rössli, M. P. *et al.* Observation of quantum Hall interferometer phase jumps due to a change in the number of bulk quasiparticles. *Phys. Rev. B* **101**, 125302 (2020).
 - ²⁶ Rosenow, B. & Halperin, B. I. Influence of Interactions on Flux and Back-Gate Period of Quantum Hall Interferometers. *Phys. Rev. Lett.* **98**, 106801 (2007).
 - ²⁷ Halperin, B. I., Stern, A., Neder, I. & Rosenow, B. Theory of the Fabry-Pérot quantum Hall interferometer. *Phys. Rev. B* **83**, 155440 (2011).
 - ²⁸ Ngo Dinh, S. & Bagrets, D. A. Influence of Coulomb interaction on the Aharonov-Bohm effect in an electronic Fabry-Pérot interferometer. *Phys. Rev. B* **85**, 073403 (2012).
 - ²⁹ Lafont, F., Rosenblatt, A., Heiblum, M. & Umansky, V. Counter-propagating charge transport in the quantum Hall effect regime. *Science* **363**, 54–57 (2019).
 - ³⁰ Bhattacharyya, R., Banerjee, M., Heiblum, M., Mahalu, D. & Umansky, V. Melting of Interference in the Fractional Quantum Hall Effect: Appearance of Neutral Modes. *Phys. Rev. Lett.* **122**, 246801 (2019).
 - ³¹ Wang, L. *et al.* One-dimensional electrical contact to a two-dimensional material. *Science* **342**, 614–617 (2013).
 - ³² Du, X., Skachko, I., Duerr, F., Luican, A. & Andrei, A. Y. Fractional quantum hall effect and insulating phase of Dirac electrons in graphene. *Nature* **462**, 192–195 (2009).
 - ³³ Bolotin, K. I., Ghahari, F., Shulman, M. D., Stormer, H. L. & Kim, P. Observation of the fractional quantum hall effect in graphene. *Nature* **462**, 196–199 (2009).
 - ³⁴ Dean, C. R. *et al.* Multicomponent fractional quantum hall effect in graphene. *Nature Physics* **7**, 693–696 (2011).
 - ³⁵ Kim, Y. *et al.* Even denominator fractional quantum Hall states in higher Landau levels of graphene. *Nature Physics* **15**, 154–158 (2018).
 - ³⁶ Zibrov, A. A. *et al.* Even-denominator fractional quantum Hall states at an isospin transition in monolayer graphene. *Nature Physics* **15**, 154–158 (2018).
 - ³⁷ Young, A. F. *et al.* Tunable symmetry breaking and helical edge transport in a graphene quantum spin hall state. *Nature* **505**, 528–532 (2014).
 - ³⁸ Veyrat, L. *et al.* Helical quantum Hall phase in graphene on SrTiO₃. *Science* **367**, 781–786 (2020).
 - ³⁹ Yankowitz, M., Ma, Q., Jarillo-Herrero, P. & LeRoy, B. J. van der Waals heterostructures combining graphene and hexagonal boron nitride. *Nature Reviews Physics* **1**, 112–125 (2019).
 - ⁴⁰ Maher, P. *et al.* Evidence for a spin phase transition at charge neutrality in bilayer graphene. *Nature Physics* **9**, 154–158 (2013).
 - ⁴¹ Ki, D.-K., Falko, V. I., Abanin, D. A. & Morpurgo, A. F. Observation of Even Denominator Fractional Quantum Hall Effect in Suspended Bilayer Graphene. *Nano Letters*

- 14, 2135–2139 (2014).
- ⁴² Li, J. I. A. *et al.* Even-denominator fractional quantum Hall states in bilayer graphene. *Science* **358**, 648–652 (2017).
- ⁴³ Huard, B. *et al.* Transport measurements across a tunable potential barrier in graphene. *Phys. Rev. Lett.* **98**, 236803 (2007).
- ⁴⁴ Veyrat, L. *et al.* Low-Magnetic-Field Regime of a Gate-Defined Constriction in High-Mobility Graphene. *Nano Letters* **19**, 635–642 (2019).
- ⁴⁵ Wei, D. S. *et al.* Mach-Zehnder interferometry using spin- and valley-polarized quantum Hall edge states in graphene. *Science Advances* **3**, e1700600 (2017).
- ⁴⁶ Makk, P. *et al.* Coexistence of classical snake states and Aharonov-Bohm oscillations along graphene p - n junctions. *Phys. Rev. B* **98**, 035413 (2018).
- ⁴⁷ Zhang, G. *et al.* Coulomb-dominated oscillations in a graphene quantum Hall Fabry-Pérot interferometer. *Chinese Physics B* **28**, 127203 (2019).
- ⁴⁸ Zimmermann, K. *et al.* Tunable transmission of quantum Hall edge channels with full degeneracy lifting in split-gated graphene devices. *Nature Commun.* **8**, 14983 (2017).
- ⁴⁹ Yamauchi, Y. *et al.* Universality of bias- and temperature-induced dephasing in ballistic electronic interferometers. *Phys. Rev. B* **79**, 161306 (2009).
- ⁵⁰ Gurman, I., Sabo, R., Heiblum, M., Umansky, V. & Mahalu, D. Dephasing of an electronic two-path interferometer. *Phys. Rev. B* **93**, 121412 (2016).
- ⁵¹ Amet, F. *et al.* Supercurrent in the quantum hall regime. *Science* **352**, 966–969 (2016).
- ⁵² Lee, G. *et al.* Inducing superconducting correlation in quantum Hall edge states. *Nature Physics* **13**, 693–698 (2017).
- ⁵³ Zhao, L. *et al.* Interference of chiral Andreev edge states. *Nature Physics* **16**, 862–867 (2020).
- ⁵⁴ Huang, X. L. & Nazarov, Y. V. Interaction-induced supercurrent in quantum Hall setups. *Phys. Rev. B* **100**, 155411 (2019).
- ⁵⁵ Clarke, D., Alicea, J. & Shtengel, K. Exotic non-Abelian anyons from conventional fractional quantum Hall states. *Nature Commun.* **4**, 1348 (2013).
- ⁵⁶ Stern, A. & Lindner, N. H. Topological Quantum Computation—From Basic Concepts to First Experiments. *Science* **339**, 1179–1184 (2013).
- ⁵⁷ Mong, R. S. K. *et al.* Universal Topological Quantum Computation from a Superconductor-Abelian Quantum Hall Heterostructure. *Phys. Rev. X* **4**, 011036 (2014).
- ⁵⁸ Liu, M. Theory of carrier density in multigated doped graphene sheets with quantum corrections. *Phys. Rev. B* **87**, 125427 (2013).
- ⁵⁹ Chklovskii, D. B., Shklovskii, B. I. & Glazman, L. I. Electrostatics of edge channels. *Phys. Rev. B* **46**, 4026–4034 (1992).
- ⁶⁰ Evans, A. K., Glazman, L. I. & Shklovskii, B. I. Coulomb blockade in the quantum-Hall-effect state. *Phys. Rev. B* **48**, 11120 (1993).
- ⁶¹ Roulleau, P. *et al.* Finite bias visibility of the electronic Mach-Zehnder interferometer. *Phys. Rev. B* **76**, 161309 (2007).
- ⁶² Roulleau, P. *et al.* Noise Dephasing in Edge States of the Integer Quantum Hall Regime. *Phys. Rev. Lett.* **101**, 186803 (2008).
- ⁶³ Litvin, L. V., Helzel, A., Tranitz, H., Wegscheider, W. & Strunk, C. Edge-channel interference controlled by Landau level filling. *Phys. Rev. B* **78**, 075303 (2008).

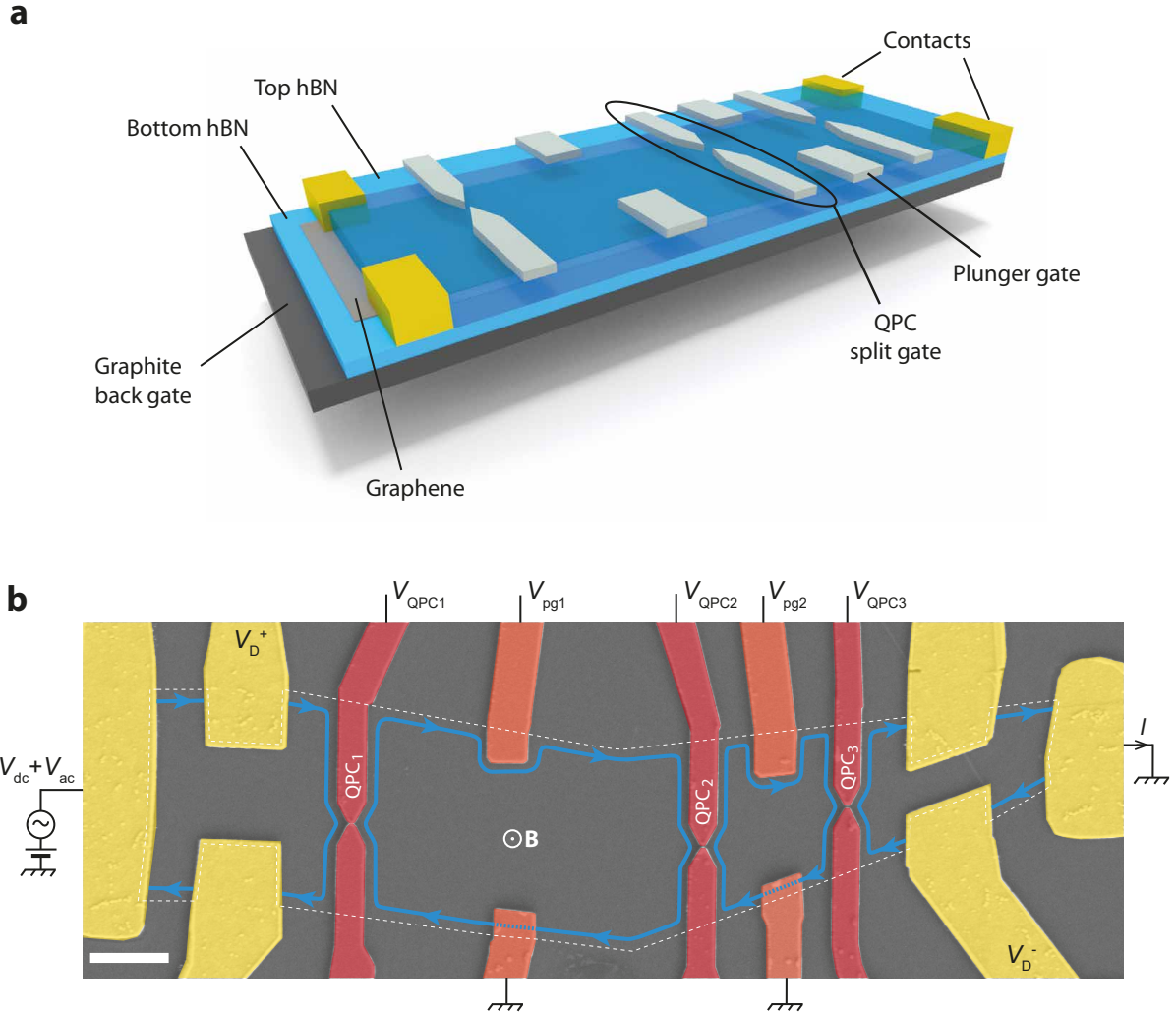


FIG. 1. **Graphene quantum Hall Fabry-Pérot interferometer.** **a**, Schematic of the van der Waals hBN/graphene/hBN/graphite heterostructure equipped with split-gate and plunger-gate electrodes (light gray) atop it. The graphite flake serves as back-gate electrode and the graphene is contacted through edge contacts³¹ (yellow). Further details about nanofabrication are given in Methods. **b**, False-colored scanning electron micrograph of the device. The scale bar is 1 μm . Three QPCs define two FP cavities. The interfering quantum Hall edge channel (blue line) propagates along the graphene edges (white dashed line), and along the split-gate (red) and plunger-gate (orange) electrodes, illustrating a configuration in which the gate electrodes deplete the charge carriers and repel the quantum Hall edge channel. The transmissions of the FP cavities are measured through the diagonal differential resistance $R_D = dV_D/dI$, where I is the current measured by an ammeter and V_D the diagonal voltage drop across the contacts V_D^+ and V_D^- , in voltage bias configuration using a dc and ac voltage sources, V_{dc} and V_{ac} .

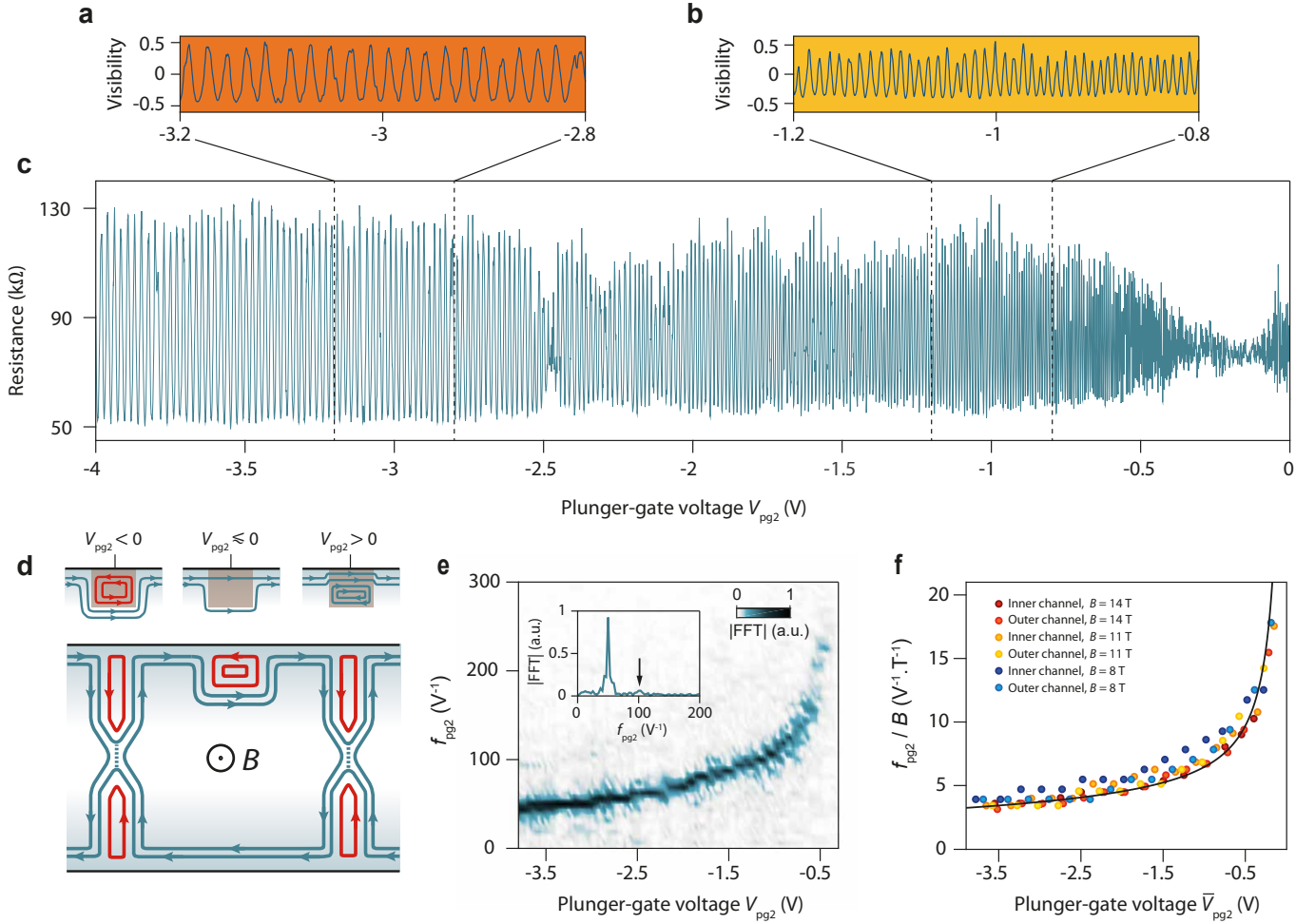


FIG. 2. Gate-tunable quantum interference. **a, b, c,** Diagonal resistance oscillations as a function of plunger-gate voltage V_{pg2} measured on the small interferometer at 0.015 K and 14 T (with an ac bias voltage of $5 \mu\text{V}$). The back-gate voltage is set to $V_{bg} = 0.533 \text{ V}$ corresponding to a filling factor $\nu_b = 1.5$ in the bulk. The split-gate voltages on QPC₂ and QPC₃ are tuned to obtain partial transmission of the outer edge channel. The charge neutrality point below the plunger gate is at -0.3 V and corresponds to a suppression of the oscillation amplitude in **c** due to the divergence of the oscillation frequency shown in **e**. **a** and **b** show zooms on smaller V_{pg2} ranges of the resistance oscillations converted in visibility $(R - \bar{R})/\bar{R}$, where \bar{R} is the resistance average. **d,** Schematics of the QH-FP interferometer illustrating the edge channels configuration for the measurements in **c**. The black lines represent the physical edges of graphene. The blue (red) lines indicate electron(hole)-like edge channels and the arrows the direction of motion of charge carriers. At the QPC constriction, the dashed line indicates the tunneling of the interfering edge channel. Top sketches: Three configurations for the states around the plunger gate. Left, accumulation of localized hole states repelling the propagating electron edge channels. Middle, depletion of charge carrier density to a filling factor 1 below the gate, which repels the inner edge channel. Right, accumulation of localized electron states that push the propagating edge channels closer to the graphene edge. **e,** Fourier amplitude of the resistance oscillations in **c** as a function of V_{pg2} and the plunger-gate-voltage frequency f_{pg2} obtained by computing the Fourier transform over a small V_{pg2} window of 0.16 V sliding over the whole V_{pg2} range. Inset: Fourier transform at $V_{pg2} = -3.28 \text{ V}$ showing a well-defined peak at $f_{pg2} = 50 \text{ V}^{-1}$ and a faint peak at $f_{pg2} = 100 \text{ V}^{-1}$ indicated by the black arrow. These peaks correspond to first order and second order (two turns in the FP loop) interference processes. **f,** Evolution of the main peak frequency f_{pg2} rescaled by the magnetic field B as a function of \bar{V}_{pg2} , the plunger-gate voltage shifted with respect to the voltage that expels the interfering edge channel. The plot gathers a set of experiments performed with different interfering edge states and at different magnetic fields. The collapse of all data points into a single curve is fitted by an electrostatic simulation (see Supp. Section IX) of the pn-junction displacement with plunger-gate voltage (black line).

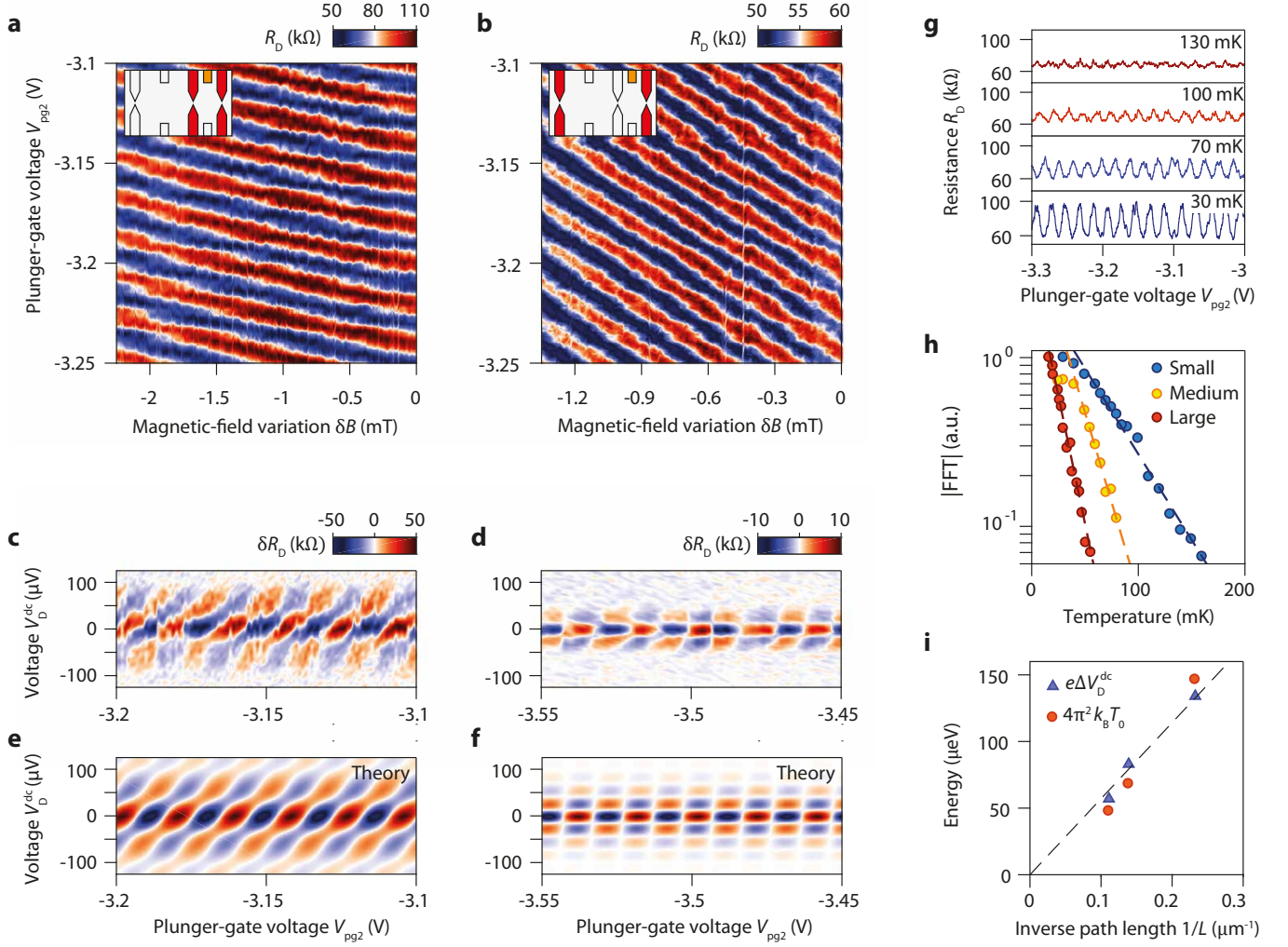


FIG. 3. Aharonov-Bohm effect and energy dependence. **a, b**, Diagonal resistance R_D versus plunger-gate voltage V_{pg2} and magnetic field variation δB measured at 0.015 K for the small interferometer in **a** and the large interferometer in **b**. The inset schematics indicate the active QPCs (in red) and plunger gates (in orange) for the respective measurements. The negative slope in the $B - V_{pg2}$ plane is a clear indicator for the Aharonov-Bohm effect in both interferometers. **c, d**, Differential diagonal resistance variations δR_D , after background subtraction, versus measured dc diagonal voltage V_D^{dc} and plunger-gate voltage V_{pg2} for the small interferometer in **c** and the large interferometer in **d**. Typical checkerboard patterns are observed with a significant tilt for the smallest interferometer revealing incomplete symmetrization of the voltage bias. **e, f**, Numerical simulations of resistance oscillations induced by voltage bias and plunger-gate voltage that reproduce the data presented in **c** and **d**, respectively. The simulation incorporates an asymmetric potential drop at the two QPCs and an out-of-equilibrium decoherence factor (see Supp. Section XV). The asymmetry factor is $x = 0.2$ in **e** and $x = 0.02$ in **f**. **g**, Temperature evolution of the resistance oscillations versus plunger-gate voltage V_{pg2} for the small interferometer. **h**, Exponential decays of the Fourier amplitude of the resistance oscillations for the small (blue), medium (yellow) and large (red) interferometers. The dashed line is a fit with $\exp(-T/T_0)$ giving $T_0 = 43, 20,$ and 14 mK for the small, medium, and large interferometers, respectively. **i**, Evolution of the energy scales as a function of the inverse of the cavity length L of the three interferometers. The oscillation period with the dc voltage, ΔV_D^{dc} , of the checkerboard pattern corresponds to the Thouless energy E_{Th} and is expected to be equal to the energy scale $4\pi^2 k_B T_0$ of the temperature-induced blurring of the resistance oscillations⁴. The dashed line is a linear fit highlighting the $1/L$ scaling of both energy scales. All data in this figure are obtained in a configuration with the outer edge channel interfering at $B = 14$ T.

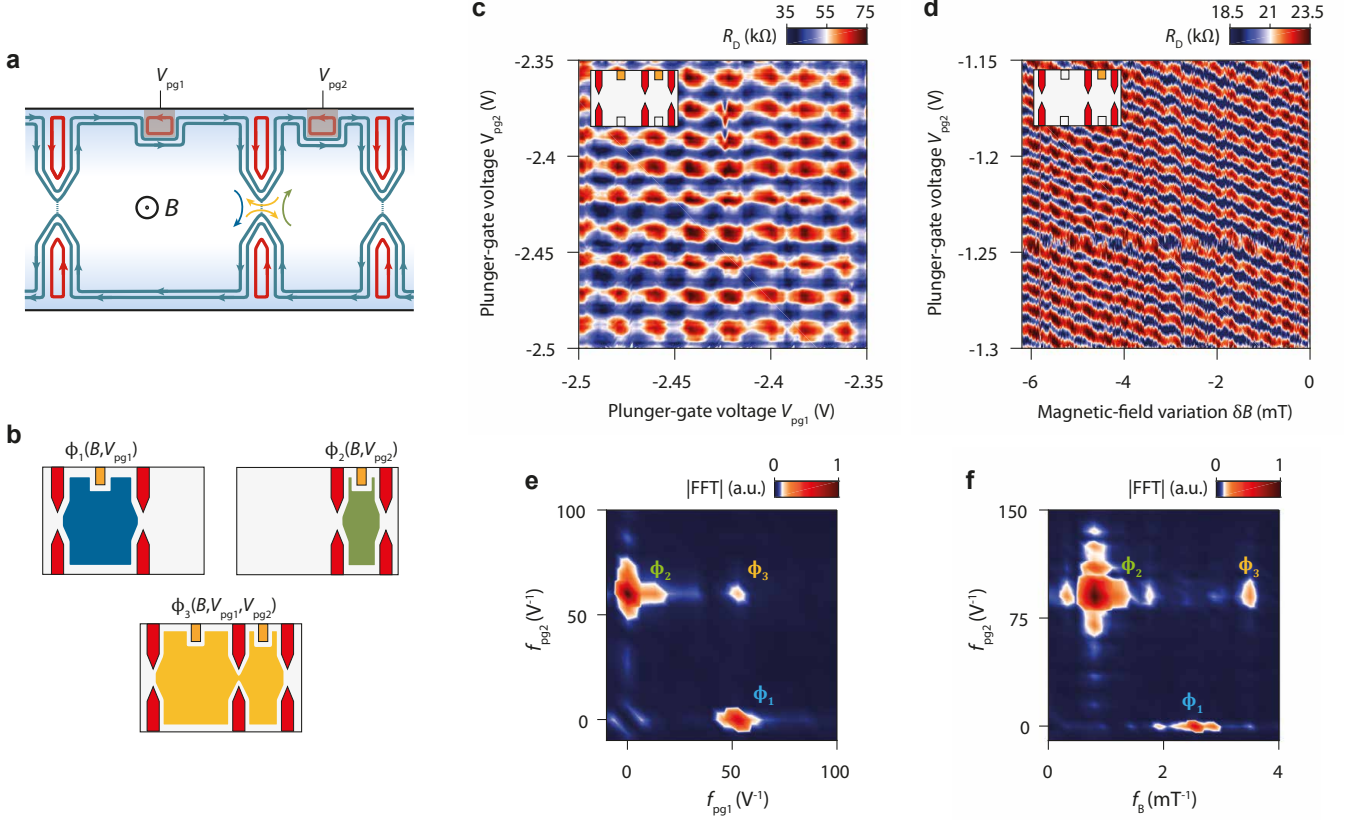


FIG. 4. Coherently-coupled double QH-FP interferometer. **a**, Schematics of the double QH-FP interferometer in a configuration of partial backscattering of the inner edge channel at the three QPCs. The central QPC can either reflect an incoming electron from the left cavity (blue arrow) or the right cavity (green arrow), or transmit coherently an electron from one cavity to the other (yellow arrows). In the latter case, electrons pick up the Aharonov-Bohm phase given by the combined areas of the small and medium interferometers. **b**, Schematics of the cavities involved in the different interference processes depicted in **a**. $\phi_{1,2,3}$ are the corresponding Aharonov-Bohm fluxes, indicated with the magnetic field and plunger-gate voltages that modulate them. **c**, Diagonal resistance versus plunger-gate voltages V_{pg1} and V_{pg2} (outer edge channel interfering, $B = 14$ T). **d**, Diagonal resistance R_D versus magnetic field variation δB and plunger-gate voltage V_{pg2} (inner edge channel interfering, $B = 14$ T). The inset schematics in **c** and **d** indicate the active QPCs (in red) and plunger gates (in orange) for the respective measurements. **e**, Fourier amplitude of the resistance oscillations in **c** versus plunger-gate-voltage frequencies f_{pg1} and f_{pg2} . The three peaks at $(f_{pg1}, f_{pg2}) = (53 \text{ V}^{-1}, 0 \text{ V}^{-1})$, $(0 \text{ V}^{-1}, 60 \text{ V}^{-1})$ and $(53 \text{ V}^{-1}, 60 \text{ V}^{-1})$ correspond to the three Aharonov-Bohm fluxes depicted in **b**. **f**, Fourier amplitude of the resistance oscillations in **d** versus magnetic field frequency f_B and plunger-gate-voltage frequency f_{pg2} . The three peaks of the three Aharonov-Bohm fluxes emerge at $(f_B, f_{pg2}) = (0.79 \text{ mT}^{-1}, 90 \text{ V}^{-1})$, $(2.54 \text{ mT}^{-1}, 0 \text{ V}^{-1})$ and $(3.49 \text{ mT}^{-1}, 90 \text{ V}^{-1})$. In both Fourier amplitude maps, the peak that corresponds to flux $\phi_3(B, V_{pg1}, V_{pg2})$ reveals the quantum coherence throughout the two cavities of the double QH-FP interferometer.

Supplementary Information

I. SAMPLES STUDIED

Figure S1 displays optical images of the devices studied in this work. The fabrication process is described in Methods. The thickness of the van der Waals layers and the size of the split-gate gaps are reported in Table I.

Sample	Top hBN thickness (nm)	Bottom hBN thickness (nm)	Graphite thickness (nm)	Split-gate gap (nm)
BNGr74	22	18	4	0 / 21 / 20
BNGr64	20	50		148 / 159
BNGr30	25	15		129 / 140

TABLE I. **Samples characteristics.** The thickness of the hBN and graphite layers are measured by atomic force microscopy. The gap size of the split-gate electrodes is measured by scanning electron microscopy.

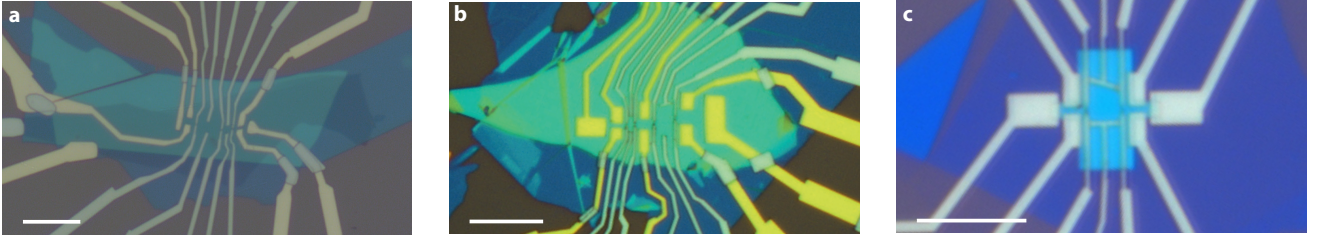


FIG. S1. **Optical images of the devices.** **a**, Sample BNGr74 of the main text. **b**, Sample BNGr64 described in section XIII. **c**, Sample BNGr30 described in section XIII. Scale bars are 10 μm .

II. PARAMETERS EXTRACTED FROM THE AHARONOV-BOHM INTERFERENCE

Table II presents the various parameters extracted from the measurements shown in Figure 3 of the main text, among which the Aharonov-Bohm period $\Delta B_{@14\text{T}}$, the Thouless energy E_{Th} extracted from the checkerboard patterns, the energy scale T_0 related to the temperature dependence of the resistance oscillation, together with the geometrical dimensions (surfaces and lengths between QPCs) of the three Fabry-Pérot cavities.

Importantly, we stress that the determination of the device geometry relies on optical images of the graphene flake taken during the van der Waals pick up process, which makes the exact determination of the graphene edge delicate. We therefore assess the graphene edge position from this image at ± 150 nm, which results in the uncertainties of the geometrical area A_{geo} of the FP cavities and lengths L between QPCs reported in Table II.

QH-FP	$\Delta B_{@14\text{T}}$ (mT)	A_{AB} (μm^2)	A_{geo} (μm^2)	L (μm)	E_{Th} (μV)	T_0 (mK)	$E_{\text{Th}}/4\pi^2 k_{\text{B}}$ (mK)
Small	1.32	3.1	3.1 ± 0.4	4.3 ± 0.5	134	43	39
Medium	0.40	10.4	10.7 ± 1.2	7.2 ± 0.5	83	20	24
Large	0.27	15.0	13.1 ± 1.8	9.0 ± 0.5	57	14	17

TABLE II. **Geometrical and physical parameters corresponding to the measurements of Fig. 3** Aharonov-Bohm period $\Delta B_{@14\text{T}}$ obtained at $B = 14$ T and resulting Aharonov-Bohm area A_{AB} ; geometrical area A_{geo} of the FP cavities; geometrical length L between two QPCs of the cavity; Thouless energy E_{Th} extracted from the checkerboard patterns in Fig. 3c and d; Energy scale T_0 extracted from Fig. 3h; $E_{\text{Th}}/4\pi^2 k_{\text{B}}$, the quantity theoretically equal to T_0 according to ref.⁴

III. DESIGN CHARACTERISTIC OF THE QPCS

The presence of the graphite back-gate electrode separated from the graphene by a thin hBN dielectric layer imposes drastic conditions for the design of the split-gate electrodes. Contrary to devices on Si/SiO₂ studied in ref.^{44,48} in which the split-gate gap of about 150 nm led to a suitable ratio of split-gate capacitance to QPC capacitance, the very close proximity of the graphite back gate imposes a much smaller split-gate gap. By performing numerical simulations⁴⁴, we estimated the split-gate gap that leads to a ratio of split-gate capacitance to QPC capacitance of the order of 2 to be of the order of few tens of nanometers, depending on the hBN thicknesses. Figure S2 displays scanning electron micrographs of the three split gates of sample BNGr74 discussed in the main text. The split-gate gaps of QPC₂ and QPC₃ are 20 nm, suitable for operating the split gates as QPCs in the quantum Hall regime. The split-gate electrodes of QPC₁ are unintentionally connected but this short-circuit does not hinder QPC operation (see QPC characterizations in section VI).

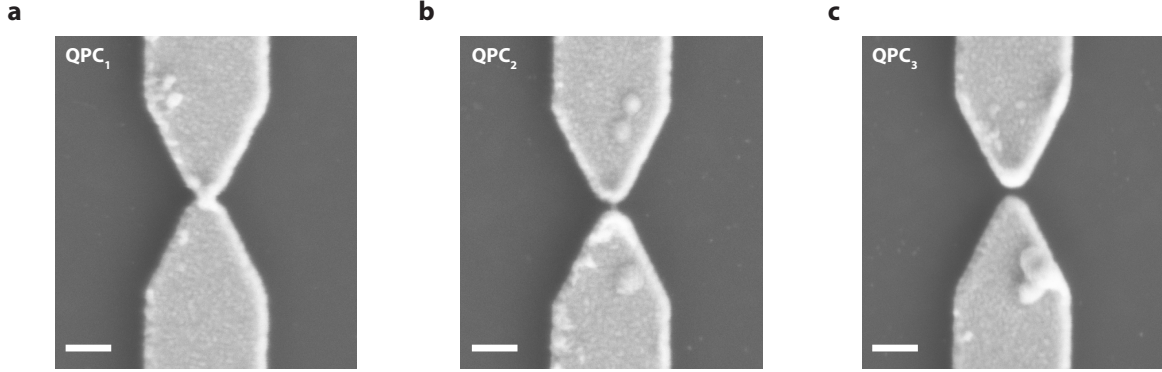


FIG. S2. **QPCs geometry.** Scanning electron micrograph of the QPCs of BNGr74 device. **a**, QPC₁. **b**, QPC₂. **c**, QPC₃. The two split-gate electrodes of QPC₁ are unintentionally connected. The gaps between the two other split gates is 20 nm. Scale bar is 100 nm.

IV. CHARACTERIZATION OF THE SPLIT-GATE CAPACITANCES AT 0 T

In this section, we present the characterization of the back gate and the different split gates at zero magnetic field for the sample of the main text. Figure S3 shows color-coded maps of the longitudinal resistance R_{xx} versus back-gate voltage V_{bg} and voltage V_{QPC} applied on a split gate (other split gates are floating). The maps exhibit four quadrants separated by two nearby horizontal lines and a diagonal line. The most resistive horizontal line, at $V_{bg} = -0.04$ V, corresponds to the charge neutrality point in the bulk of graphene and the diagonal line corresponds to the charge neutrality point below the active split-gate electrodes, as usual for graphene devices equipped with a local top gate. The two lines intersect at $V_{QPC} \simeq +0.38$ V as a result of the work function difference between the palladium of the gates and the graphene. The second horizontal line is more unusual and results from the local hole doping of the graphene beneath the two other split gates that are not active but contribute in series to the measured resistance. The palladium of these split-gate electrodes shifts the position of the charge neutrality point beneath them to $V_{bg} = 0.12 - 0.18$ V, yielding a secondary resistance peak, independent of the active split gate and observed consistently for the three QPC maps. These maps also provide the capacitance ratios C_{sg}/C_{bg} between the active split-gate and the back-gate electrodes which are respectively 0.83 for QPC₁ and 0.86 for QPC₂ and QPC₃. They are important quantities for the analysis of the QPC properties in the QH regime.

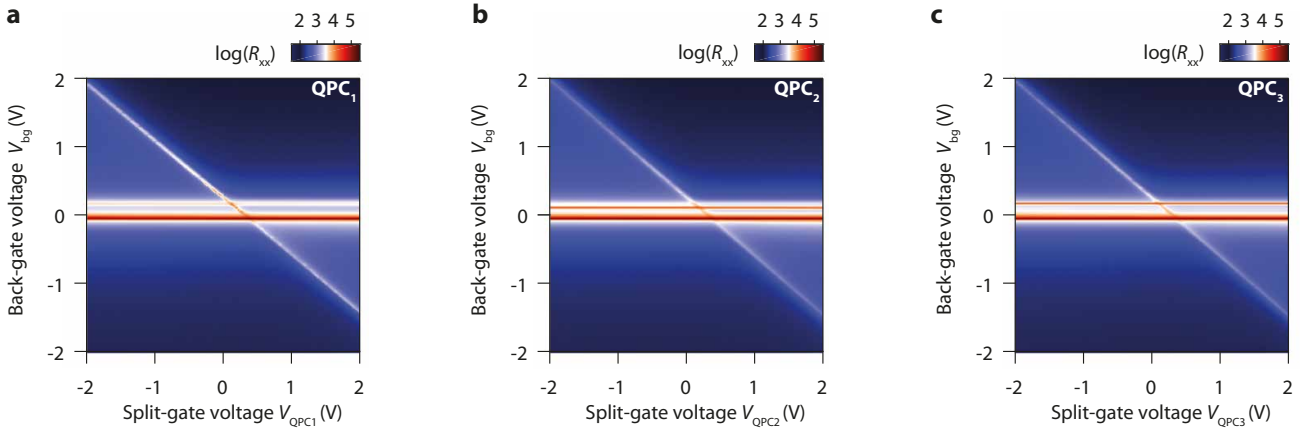


FIG. S3. **Split-gates characterization at 0 T.** **a, b, c,** Longitudinal resistance R_{xx} versus split-gate voltage V_{QPC} and back-gate voltage V_{bg} for the three QPCs of the QH-FP interferometer presented in the main text. The horizontal line at $V_{bg} = -0.04$ V corresponds to the charge neutrality point in the bulk graphene, whereas the diagonal lines correspond to the charge neutrality point in the graphene beneath the active split gate. These lines intersect at $(V_{QPC}, V_{bg}) \simeq (+0.38$ V, -0.04 V) revealing the significant local hole doping induced by the palladium gates. The second horizontal line at $V_{bg} = 0.18$ V in a and c and $V_{bg} = 0.12$ V in b marks the positive back-gate voltage needed to compensate the hole doping induced by the palladium beneath the non-active split gates.

V. FAN DIAGRAM OF BULK LANDAU LEVELS

In this section, we present the Landau fan diagram of sample BNGr74. Fig. S4 displays the longitudinal resistance R_{xx} as a function of magnetic field B and back-gate voltage V_{bg} , measured at 0.02 K. This measurement was performed with a voltage $V_{QPC} = +0.3$ V applied on each QPC to compensate the hole doping induced by the palladium split gates and ensure a quasi-homogeneous charge carrier density in the graphene layer.

Broken-symmetry states in electron(hole)-type Landau levels emerge as minima in R_{xx} above 5 T (3 T), consistent with the mobility $\mu = 130\,000\text{ cm}^2\cdot\text{V}^{-1}\cdot\text{s}^{-1}$ obtained for a charge carrier density of $1 \times 10^{12}\text{ cm}^{-2}$ from Hall measurements. In addition, an insulating behaviour develops at charge neutrality with increasing magnetic field. The full-lifting of the degeneracies in the zeroth Landau level occurs above 4 T, allowing to perform interferometry experiments with the inner or outer electron edge channels of the zeroth Landau level at relatively low magnetic field values (see section XII).

From the position of the R_{xx} minima, we extract a back-gate capacitance $C_{bg} = 1.45\text{ mF/m}^2$ consistent with the bottom hBN thickness and a hBN dielectric constant $\epsilon_r^{\text{BN}} \approx 3$.

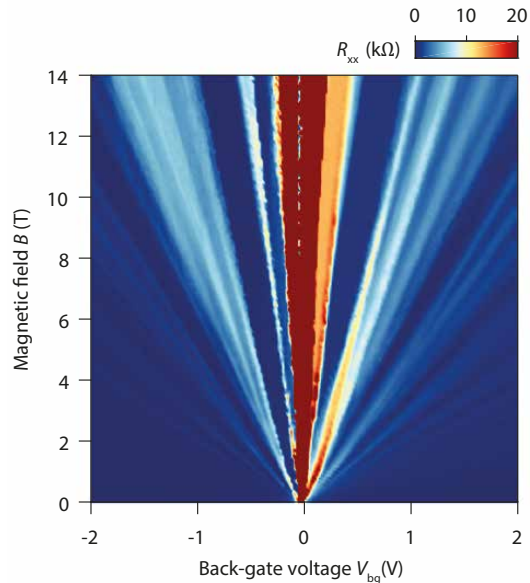


FIG. S4. **Landau fan diagram.** Longitudinal resistance R_{xx} of sample BNGr74 (device of the main text) versus back-gate voltage V_{bg} and magnetic field B , measured at 0.02 K.

VI. CHARACTERIZATION OF THE QPCS IN THE QUANTUM HALL REGIME

QH interferometry experiments require a precise knowledge of the edge-channels configuration in the bulk of graphene, beneath the split-gate electrodes and in the split-gate constrictions. This section describes the action of the split-gate electrodes in the QH regime, which allows to determine the gate-voltage set points for the (partial) QPC pinch-off and tuning of QH edge channel transmissions.

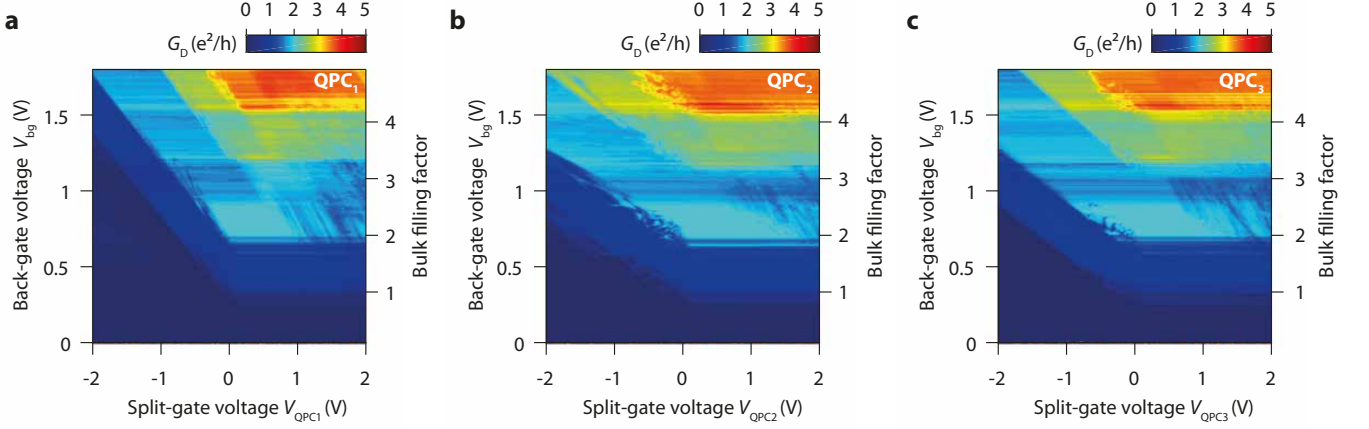


FIG. S5. **QPC conductance maps at 14 T.** **a, b, c,** Diagonal conductance G_D versus split-gate voltages, V_{QPC} , and back-gate voltages, V_{bg} , for the three QPCs of the device presented in the main text. During a measurement, only one QPC is studied and the two other sets of split gates are kept floating. The slope of the diagonal stripes corresponds to the capacitance ratio between the QPC constriction and the back gate. This slope is about twice/three times smaller than the zero-field slope for QPC₂ and QPC₃, but is only slightly smaller for QPC₁ (due to the unintentional absence of gap between the two electrodes of this QPC).

Figure S5 displays the diagonal conductance G_D as a function of split-gate and back-gate voltages, V_{QPC} and V_{bg} , for the three QPCs. The three conductance maps show features similar to those reported in ref.⁴⁸ for a QPC operating in the QH regime. At negative split-gate voltages, G_D draws diagonal strips of nearly constant and quantized values. They have a smaller slope than the zero-field diagonal lines of Fig. S3, indicative of the smaller couplings at the constrictions characterized by capacitance ratios $C_{QPC}/C_{bg} \simeq 0.58, 0.31$ and 0.36 for QPC₁, QPC₂ and QPC₃, respectively. As demonstrated in ref.⁴⁸, the quantized G_D values indicate the number of transmitted QH edge channels through the QPC. For a given bulk filling factor, the QH edge channels can be backscattered by applying a negative split-gate voltage V_{QPC} . For instance, at $V_{bg} = 0.75$ V, the bulk filling factor is $\nu \simeq 2$, leading to the blue rhombi of $G_D = 2e^2/h$ located near $V_{QPC} = 0$ V in Fig. S5. Decreasing V_{QPC} to negative values, the conductance drops to the dark blue strip of $G_D = e^2/h$, and then to $G_D = 0$ at even more negative values. These conductance changes reflect the successive backscattering of the QH edge channels at the QPC⁴⁸. The linecuts of Fig. S6 further illustrate such a successive pinch off of the inner and outer edge channels at $\nu \simeq 2.5$ (Fig. S6a) and the pinch off the outer edge channel at $\nu \simeq 1.5$ (Fig. S6b).

As discussed in section IV, the hole-doped graphene regions beneath the non active split-gate electrodes intervene in the transmission of the whole device when studying the properties of a particular split gate. These hole-doped regions have a lower filling factor than the bulk and can therefore backscatter some bulk QH edge channels. As a consequence, the QH plateaus as a function of back-gate voltage at $V_{QPC} \sim 0$ V in the QPC maps of Fig. S5 are not centered at the integer bulk filling factors indicated on the right axis and determined by the fan diagram $R_{xx}(V_{bg}, B)$ at compensated split-gate voltages (see Fig. S4).

The comparison in Fig. S7 between a QPC map and the transverse Hall resistance R_{xy} that relates to the bulk filling factor bears out this observation. The $\nu = 2$ plateau develops at lower back-gate voltage in the Hall resistance than in the diagonal resistance across the QPCs. Despite the fact that the bulk has two QH edge channels when $1/R_{xy} = \frac{2e^2}{h}$ at, for instance, $V_{bg} = 0.5$ V, the non active QPCs that have lower filling factors backscatter the inner edge channel leading to $G_D = e^2/h$ in the QPC conductance map.

Furthermore, for the data presented in the main text, we assessed the number of bulk QH edge channels through the value of the Hall resistance plateau. For all figures of the main text, we measured $1/R_{xy} = \frac{2e^2}{h}$, which indicates that two edge channels propagate in the graphene bulk.

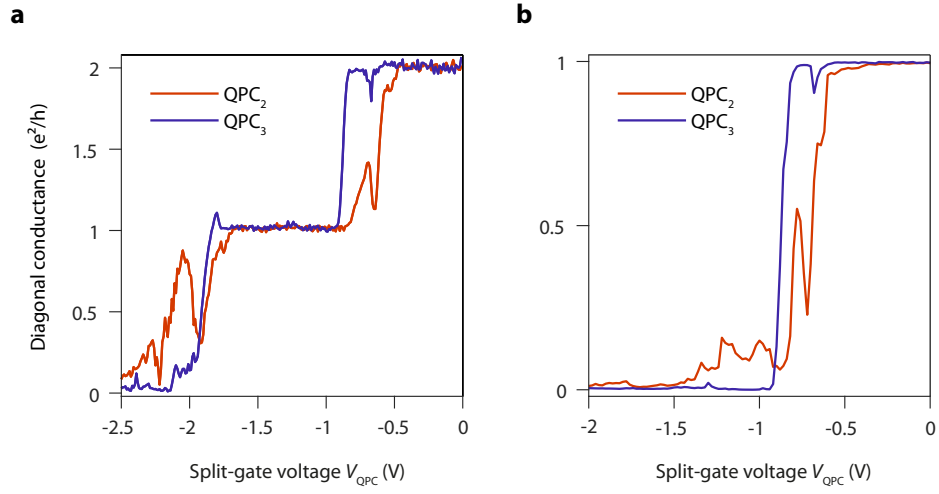


FIG. S6. **QPC transmission curves at 14 T.** Evolution of the diagonal conductance G_D as a function of split-gate voltages V_{QPC} at fixed back-gate voltage V_{bg} . **a**, $V_{bg} = 0.88$ V. **b**, $V_{bg} = 0.53$ V.

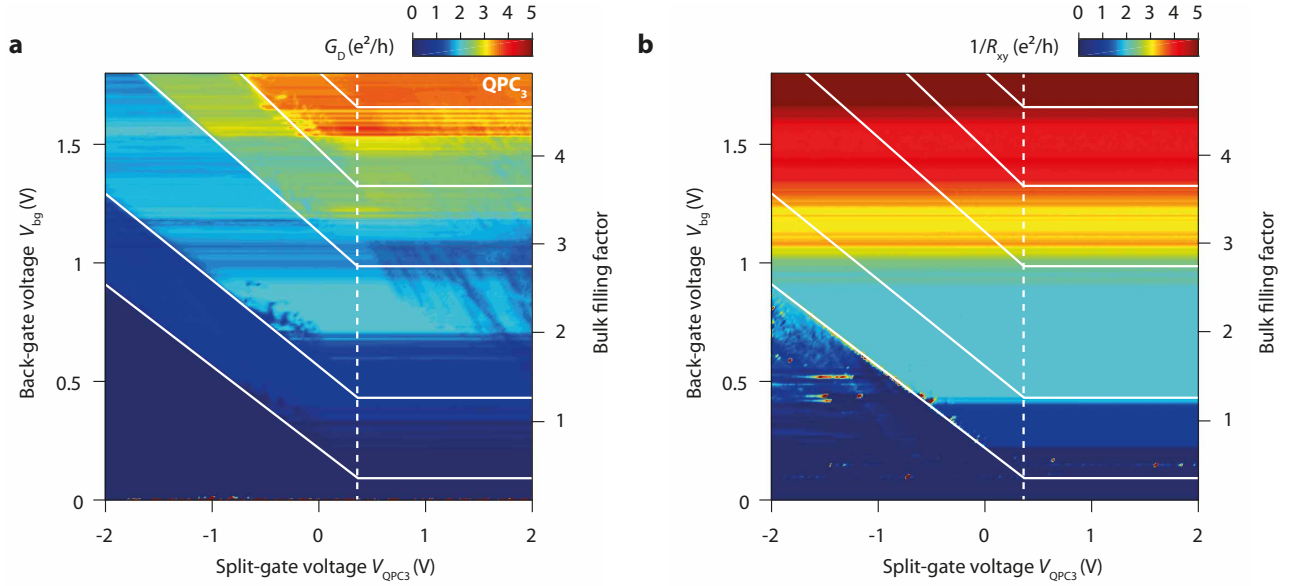


FIG. S7. **QPC map compared to Hall resistance map at 14 T.** **a**, Diagonal conductance G_D versus split-gate voltage, V_{QPC} , and back-gate voltage, V_{bg} , for QPC₃. **b**, Inverse of the transverse Hall resistance $1/R_{xy}$ versus V_{QPC} and V_{bg} . The vertical dashed white line indicates the split-gate voltage that compensates the hole doping induced by the split-gate electrodes (iso-density in the bulk and beneath the active split gate). This voltage is determined in the zero-field maps of Fig. S3 at the intersection between the diagonal line and the main horizontal line of the bulk charge neutrality point. The horizontal solid white lines delineate the quantized plateaus in the Hall resistance that are centered at integer bulk filling factors (indicated on the right axis). The diagonal lines delineate the diagonal strips of constant G_D in the QPC map, that is, conductance plateaus given by the number of transmitted edge channels through the QPC (see ref.⁴⁸ for a detailed analysis). For consistency, these diagonal lines meet the horizontal ones of the bulk Hall resistance right at their intersect with the vertical line.

VII. AHARONOV-BOHM OSCILLATIONS AT POSITIVE PLUNGER-GATE VOLTAGE

In Fig. S8, we show the extension of the measurements performed in Fig. 2c of the main text to positive plunger-gate voltage. This corresponds to the accumulation of localized electron states beneath the plunger gate (see inset in Fig. 2c). Resistance oscillations appear clearly on the positive voltage range but with an irregular shape contrary to the oscillations at $V_{pg2} < 0$ V. The Fourier amplitude of these resistance oscillations is shown in Fig. S8. The frequency of the oscillations evolves non-monotonously and is poorly defined for some voltage ranges.

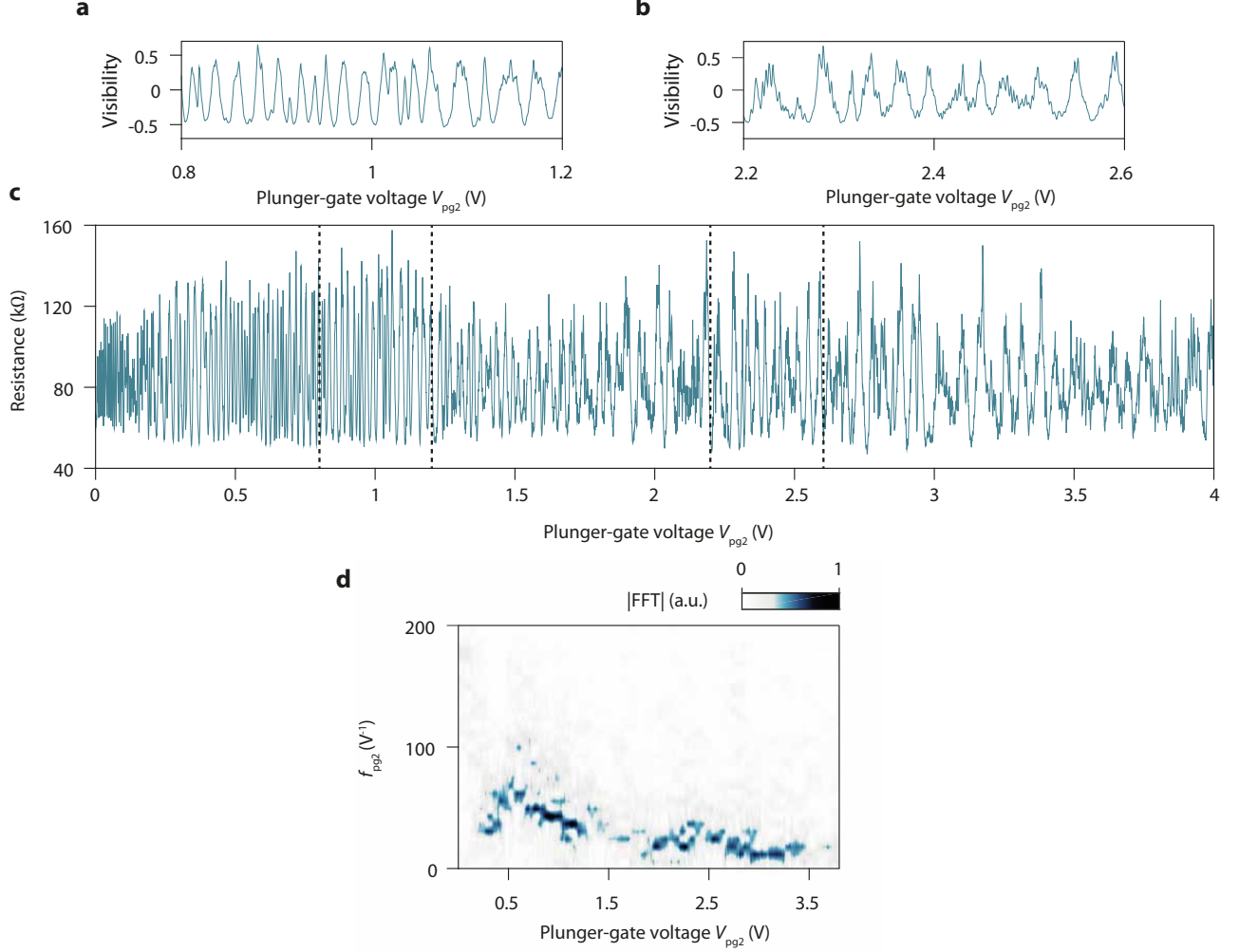


FIG. S8. **Resistance oscillations at positive plunger-gate voltage** **a, b, c**, Resistance oscillations as a function of plunger-gate voltage V_{pg2} measured in the small interferometer for $V_{pg2} > 0$. **a** and **b** show zooms on smaller V_{pg2} ranges of the resistance oscillations converted in visibility $(R - \bar{R})/\bar{R}$, where \bar{R} is the resistance background. **d**, Fourier amplitude of the resistance oscillations in **c** as a function of V_{pg2} and the plunger-gate voltage frequency f_{pg2} .

VIII. AHARONOV-BOHM OSCILLATIONS FOR DIFFERENT CONFIGURATIONS OF MAGNETIC FIELD AND EDGE CHANNELS

In this section we present plots of the Fourier amplitude of the resistance oscillations with V_{pg2} for experiments performed with different interfering edge channels and magnetic fields. In every cases, the frequency of the oscillations f_{pg2} is well defined and shows a clear and continuous decrease while lowering V_{pg2} . As expected for the Aharonov-Bohm regime, the frequency of the oscillations increases with the magnetic field at fixed plunger-gate voltage whereas it does not change with the interfering edge channel. A significant component oscillating at twice the Aharonov-Bohm frequency is visible on Fig. S9a. In this case, only the lowest frequency component was used to plot Fig. 2e in the main text.

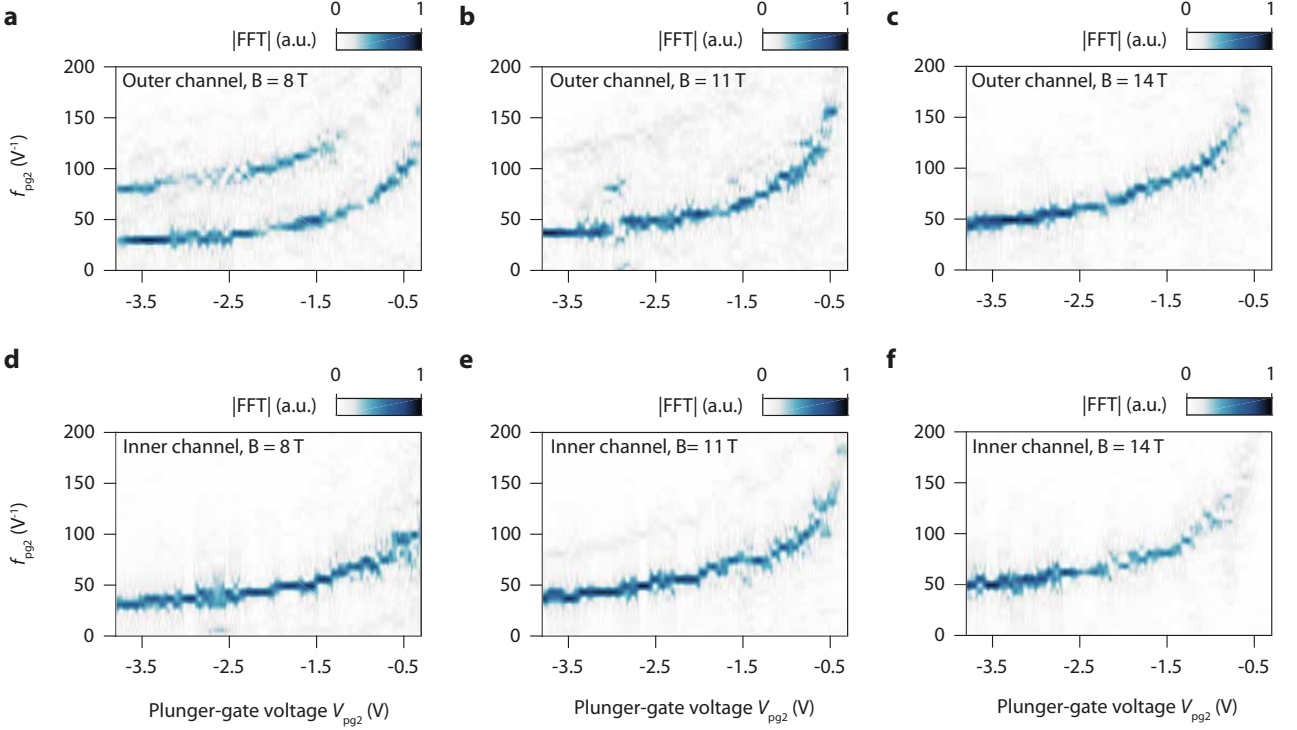


FIG. S9. **Fourier amplitude of the resistance oscillations.** Fourier amplitude of the resistance oscillations observed in the small interferometer for different configurations of magnetic field and interfering edge channel, as a function of plunger-gate voltage V_{pg2} and frequency f_{pg2} .

IX. ELECTROSTATICS OF THE PLUNGER GATE

The potential profile in the graphene below the plunger gate is determined by self-consistent electrostatic simulations in the vertical 2D plane shown in Fig. S10a assuming translational invariance in the third direction. The simulation is done for the same hBN thicknesses as in the device of the main text, with $d_{\text{bottom}} = 18$ nm for the bottom layer and $d_{\text{top}} = 22$ nm for the top layer. The hBN dielectric permittivity $\epsilon_r^{\text{BN}} \approx 3$ is extracted from the position of quantum Hall plateaus versus back-gate voltage. The graphite back-gate is treated as a perfect metal. The graphene sheet is modelled by a charge density $\sigma(x)$ linked to the electrostatic potential $V(x)$ by the relation:

$$\sigma(x) = (-e) \text{sign}(V(x)) \frac{e^2 V(x)^2}{\pi \hbar^2 v_F^2}$$

where $v_F = 10^6$ m/s is the Fermi velocity in graphene. The electrostatic problem is solved self-consistently using a modified version of MaxFEM (<http://www.usc.es/en/proyectos/maxfem>), an electromagnetic simulation software based on the finite-element method. The mesh grid computed using Gmsh (<http://gmsh.info>) extends $1 \mu\text{m}$ in vertical and $2 \mu\text{m}$ in horizontal.

The self-consistent solution $V(x)$ can be calculated for a given back-gate voltage V_{bg} and a series of plunger-gate voltages V_{pg} in order to determine the dependence of the pn interface position x_{pn} on the plunger-gate voltage. Equivalently, the local plunger-gate capacitance $C_{\text{pg}}(x)$ can be extracted from a single self-consistent simulation (for example at $V_{\text{bg}} = 0$ and $V_{\text{pg}} = -1$ V) using the quantum capacitance model⁵⁸. This model is based on the relation between $\sigma(x)$ and $V(x)$ given above, together with the definition of the capacitive couplings:

$$\sigma(x) = -C_{\text{bg}} (V_{\text{bg}} - V(x)) - C_{\text{pg}}(x) (V_{\text{pg}} - V(x))$$

where $C_{\text{bg}} = \epsilon_0 \epsilon_r^{\text{BN}} / d_{\text{bottom}}$. This approach based on the determination of the local capacitance $C_{\text{pg}}(x)$ has the advantage to provide the self-consistent solution for any set of back-gate and plunger-gate voltages without the need to solve again the full electrostatic problem.

The spatial variation of the potential energy $E(x) = -eV(x)$ below the plunger gate is plotted in Fig. S10b for a fixed back-gate voltage $V_{\text{bg}} = 0.53$ V and various negative plunger-gate voltages corresponding to the experiment reported in Fig. 2 of the main text. The position x_{pn} of the pn interface with respect to the gate edge is plotted in Fig. S10c as a function of the plunger-gate voltage, showing the following behavior: the formation of the pn interface occurs at $V_{\text{pg}} = -0.65$ V (in the data this happens around $\simeq -0.3$ V instead, due to the hole doping of $+0.38$ V from the palladium split-gate electrodes, corresponding to the charge neutrality point below the plunger gate), then the fast displacement of the pn interface corresponds to the expulsion of the pn interface from below the plunger gate, and finally the pn interface moves slower and slower for large negative plunger-gate voltages. The displacement rate $\frac{dx_{\text{pn}}}{dV_{\text{pg}}}$ plotted in Fig. S10d is used in the main text to calculate the non-linear lever arm $\alpha = L_{\text{pg}} \times \frac{dx_{\text{pn}}}{dV_{\text{pg}}}$ of the plunger gate with contour length L_{pg} . This lever arm provides the theoretical conversion between plunger-gate voltage and interferometer area, which writes $\Delta A = \alpha \Delta V_{\text{pg}}$, and which is compared in Fig. 2f with the oscillation frequency measured experimentally. L_{pg} remains an adjustable parameter because the position of the graphene edges is known with an uncertainty of ± 150 nm. To reproduce the measurement, a plunger-gate contour $L_{\text{pg}} = 1.8 \mu\text{m}$ is used, in good agreement with the expected lithographic length of $1.5 \pm 0.3 \mu\text{m}$ (the uncertainty of the graphene edge position contributes twice).

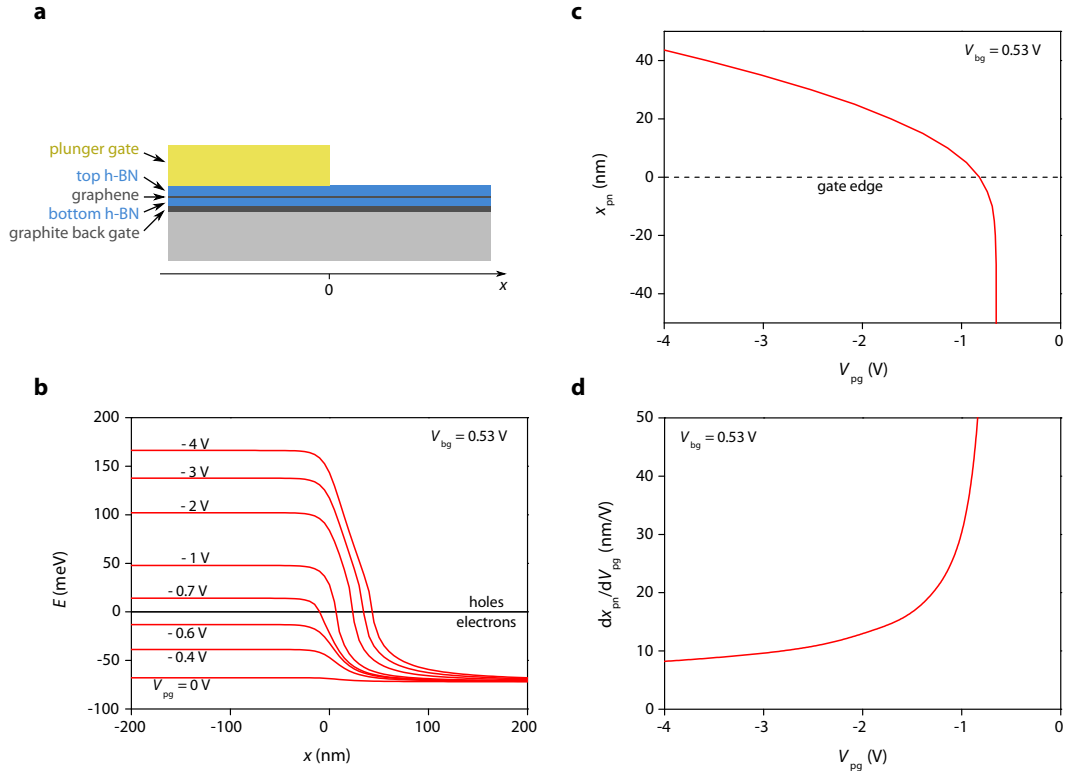


FIG. S10. **Plunger-gate electrostatics.** **a**, Schematics of the hBN/graphene/hBN heterostructure deposited on the graphite back gate and partially covered by the metallic plunger gate used to tune the interfering path length. **b**, Self-consistent electrostatic energy profiles $E = -eV$ in the graphene layer for a back-gate voltage $V_{bg} = 0.53$ V and plunger-gate voltages V_{pg} varying from 0 to -4 V. **c**, Position of the pn interface with respect to the gate edge as a function of the plunger-gate voltage. **d**, Displacement rate of the pn interface calculated as its derivative with respect to the plunger-gate voltage.

X. AHARONOV-BOHM OSCILLATIONS IN THE MEDIUM INTERFEROMETER

To complement the $(\delta B, V_{\text{pg}})$ maps shown in Fig. 3a and b for the small and large interferometers, we present in Fig. S11 the map obtained for the medium interferometer, in the same conditions, i.e. with the outer edge state at $B = 14$ T. The constant resistance lines have a negative slope indicating the Aharonov-Bohm origin of the oscillations. The field periodicity is 0.40 mT corresponding to an Aharonov-Bohm area of $10.4 \mu\text{m}^2$ in good agreement with the expected lithographic area (see Table II).

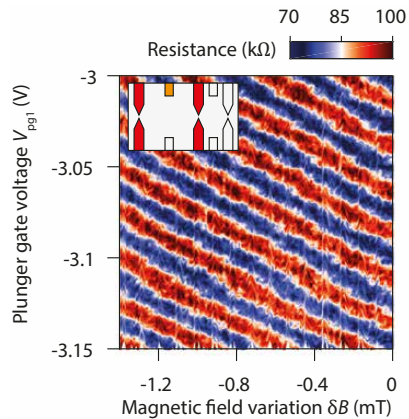


FIG. S11. **Aharonov-Bohm oscillations in the medium interferometer.** Diagonal resistance as a function of plunger-gate voltage $V_{\text{pg}2}$ and magnetic field variation δB in the medium interferometer measured at 14 T with the outer edge channel interfering. The inset schematic indicates the active QPCs (in red) and plunger gate (in orange).

XI. INTERFEROMETRY EXPERIMENTS WITH INNER EDGE STATE AT 14 T IN THE THREE INTERFEROMETERS

In this section we present additional interferometry experiments performed with the inner edge channel of the zeroth Landau level at $B = 14$ T. Fig. S12a, b and c show the diagonal resistance of the device as a function of plunger-gate voltages and magnetic field for the small, medium and large interferometers, respectively. The results are virtually identical to those performed with the outer edge channel. The magnetic field periods extracted from these measurements are respectively of 1.23, 0.39 and 0.27 mT.

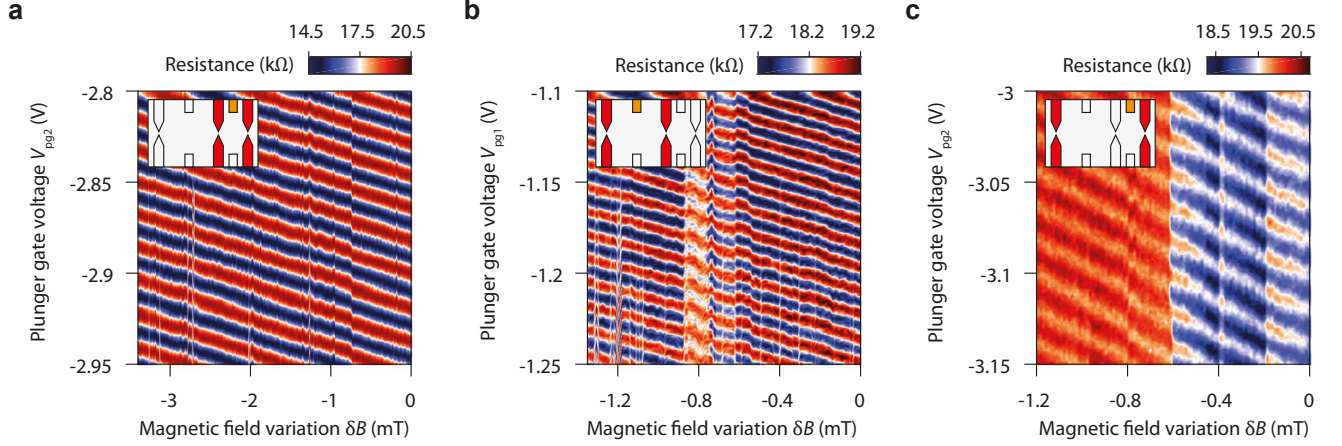


FIG. S12. **Aharonov-Bohm oscillations with the inner edge channel.** **a, b, c,** Diagonal resistance versus plunger-gate voltage $V_{pg1,2}$ and magnetic field δB for the small, medium and large interferometers, respectively, with the inner edge channel interfering at 14 T. The inset schematics indicate the active QPCs (in red) and plunger gates (in orange).

XII. INTERFERENCES AT LOWER MAGNETIC FIELDS

Here we show that the device BNGr74 presented in the main text can also operate at low magnetic field. Stable Aharonov-Bohm interference were observed with the outer and inner edge channels respectively down to 5 T and 4 T as displayed in Fig. S13a and b. The respective Fourier amplitudes of the resistance oscillations are shown in Fig. S13c and d.

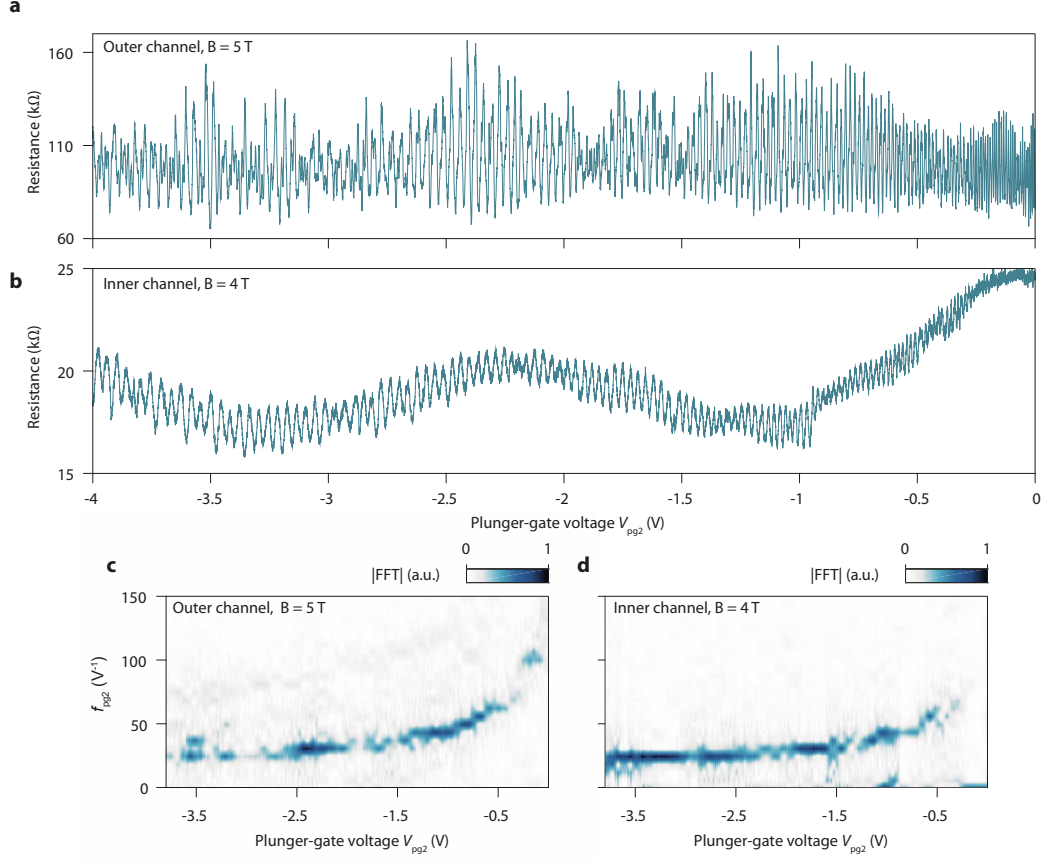


FIG. S13. **Resistance oscillations at low magnetic fields.** **a, b**, Resistance oscillations as a function of plunger-gate voltage V_{pg2} measured in the small interferometer at 5 T with the outer edge channel, and 4 T with the inner edge channel, respectively. **c, d**, Fourier amplitude of the resistance oscillations in a and b.

XIII. AHARONOV-BOHM OSCILLATIONS IN OTHER DEVICES

In this section we present the data obtained on two other devices, BNGr64 and BNGr30. They do not have a graphite back gate, and the silicon substrate serves as the back gate instead. Even without graphite electrode, we observed for both samples Aharonov-Bohm oscillations, indicating that the absence of charging effect is not only related to the screening by the graphite gate.

BNGr64 device

We first present the data for the device BNGr64 shown in Fig. S1b. In this device, three out of four QPCs were operating correctly enabling us to perform experiments with only one of the two interferometers, whose scanning electron micrograph is displayed in Fig. S14. This device was studied using a larger ac bias-voltage excitation of 20 μV and using the bottom plunger gate. The large plunger gate was kept grounded during the measurements.

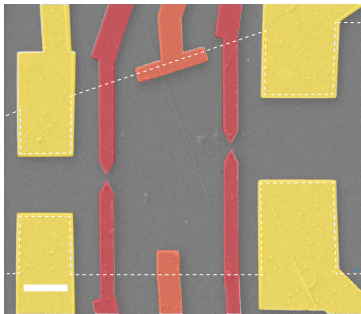


FIG. S14. **QH-FP interferometer in sample BNGr64.** False-colored scanning electron micrograph of the device. Graphene edges are represented by the white dotted line. Contacts, QPCs and plunger gates are color-coded in yellow, red and orange. Scale bar is 1 μm .

We present interferometry experiments performed with the outer interfering edge channel at 14 T with a bulk filling factor $\nu_b = 1.1$. Contrary to the data presented in the main text, there is only one electron-like edge channel propagating in the interferometer. Fig. S15c shows the evolution of the diagonal resistance with plunger-gate voltage V_{pg} . Clear resistance oscillations are observed while decreasing V_{pg} from 0 to -3.2 V. Contrary to the data presented in Fig. 2c of the main text, the oscillations show many phase shifts as well as some visibility losses, reflecting the lower degree of stability and coherence of the device. The visibility of the oscillations is typically about 15% as evidenced in Fig. S15a and b. The Fourier transform amplitude of the oscillations is presented in Fig. S15d and shows a decrease of the frequency of the oscillations f_{pg} with the plunger-gate voltage V_{pg} consistent with that in Fig. 2 of the main text.

The evolution of the diagonal resistance oscillations with both the plunger-gate voltage and the magnetic field in this configuration is shown in Fig. S15e. A smooth resistance background for each sweep was subtracted to evidence lines of constant Aharonov-Bohm phase and get rid of average-conductance variations. Constant resistance values form lines with a negative slope in the $\delta B - V_{\text{pg}}$ plane which shows that this device operates in the Aharonov-Bohm regime. From these measurements, we extract a magnetic field period of 0.42 mT corresponding to an enclosed area of 9.9 μm^2 in agreement with the geometrical surface of 11.5 μm^2 .

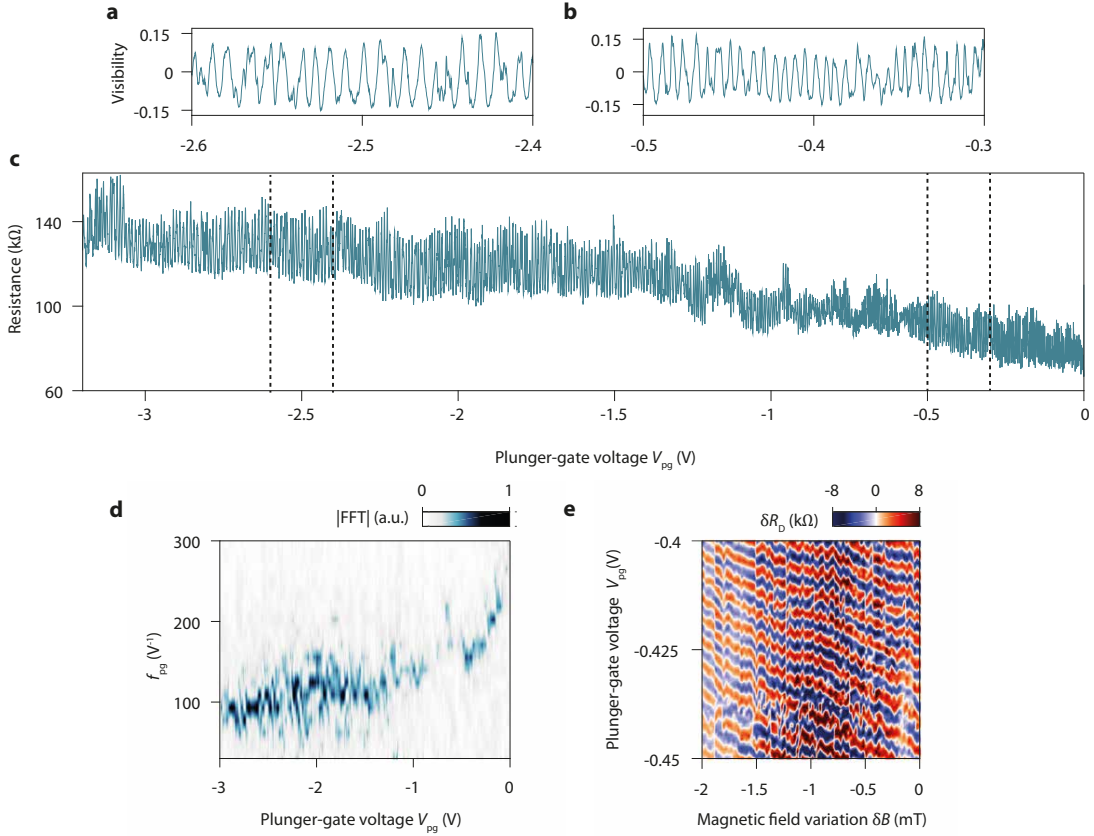


FIG. S15. **Resistance oscillations in sample BNGr64.** **a, b, c,** Resistance oscillations induced by change of the plunger-gate voltage V_{pg} in interferometry experiments with the inner edge channel at 14 T. Clear resistance oscillations are visible lowering V_{pg} , on top of a continuous increase of the mean resistance of the device evidenced in **c**. **a** and **b** show zooms on smaller V_{pg} ranges of the resistance oscillations converted in visibility $(R - \bar{R})/\bar{R}$, where \bar{R} is the resistance background. **d,** Amplitude of the Fourier transform of resistance oscillations presented in **c** with respect to the plunger-gate voltage V_{pg} and the frequency f_{pg} . A continuous decrease of the oscillations frequency is observed while decreasing V_{pg} . **e,** Evolution of the resistance oscillations as function of the plunger-gate voltage V_{pg} and the magnetic field variation δB after subtraction of a resistance background for each plunger-gate voltage sweep. Constant δR_D lines have a negative slope characteristic of oscillations induced by Aharonov-Bohm effect.

BNGr30 device

Here we present the data for the device BNGr30, displayed in Fig. S1c. Contrary to the two previous samples, before the deposition of the metallic contacts and of the gates, the heterostructure was etched and shaped using a hard-mask of HSQ resist to uncover the graphene edges at determined positions. After a second e-beam lithography steps, both the contacts and the split gates were made by depositing a Cr/Au bilayer. In this device, the plunger gates cover nearly all the graphene edges between the two QPCs. A scanning electron micrograph of the device is shown in Fig. S16.

Interferometry experiments performed in this device with the inner edge channel at bulk filling factor $\nu_b = 2.3$ and 14 T are presented in Fig. S17. Resistance oscillations induced by a change of the top plunger-gate voltage V_{pg} are shown in Fig. S17a-c. They appear on the entire range of V_{pg} voltage even though the stability of the QPC is affected by the value of V_{pg} . These oscillations have a small visibility typically varying between 2 and 5 % as shown in Fig. S17a and b. The Fourier transform analysis of the oscillations, shown in Fig. S17d reveals a similar lowering of the frequency f_{pg} of the oscillations with the plunger-gate voltage (the absence of well-defined frequency for the oscillations at $V_{pg} \simeq -1.2$ V arises from the rapid drop of the resistance background).

In Fig. S17e, we show the evolution of resistance oscillations with both the magnetic field and the plunger-gate voltage. The constant phase lines have a negative slope evidencing that the oscillations result from the Aharonov-Bohm effect. We can extract a magnetic field period of 0.37 mT corresponding to an area enclosed by the interfering edge state of $11.2 \mu\text{m}^2$ in good agreement with geometric area of $10.1 \mu\text{m}^2$.



FIG. S16. **QH-FP interferometer in sample BNGr30.** False-colored scanning electron micrograph of the device. Graphene edges are represented by the white dotted line. Contacts, QPCs and plunger gates are color-coded in yellow, red and orange, respectively. Scale bar is 1 μm .

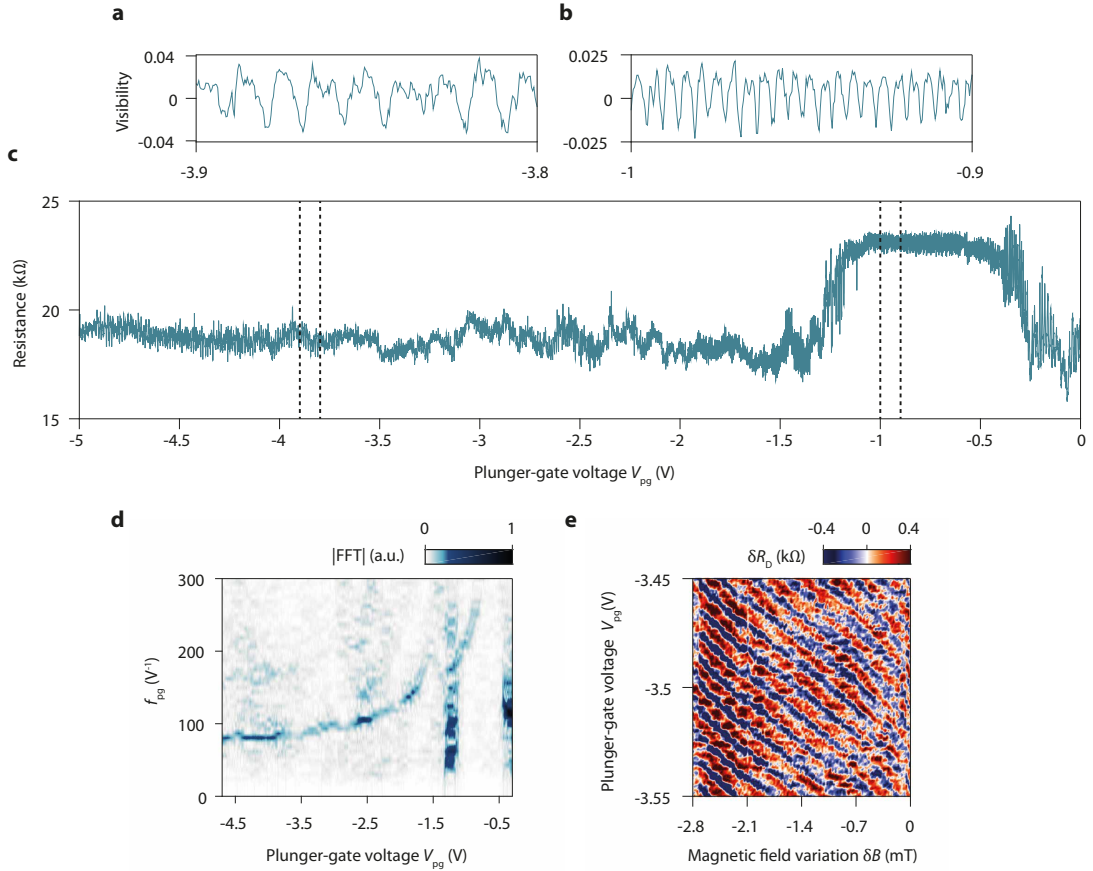


FIG. S17. **Resistance oscillations in sample BNGr30.** **a, b, c,** Resistance oscillations induced by a change of the plunger-gate voltage V_{pg} in interferometry experiments with the inner edge state at 14 T. The abrupt change in **c** of the mean resistance value at $V_{\text{pg}} \approx -1.2$ V and $V_{\text{pg}} \approx -0.2$ V might originate from instability of the QPCs. **a** and **b** show zooms on smaller V_{pg} ranges of the resistance oscillations converted in visibility $(R - \bar{R})/\bar{R}$, where \bar{R} is the resistance background. **d,** Amplitude of the Fourier transform of resistance oscillations presented in **c** with respect to the plunger-gate voltage V_{pg} and the corresponding voltage frequency f_{pg} . A continuous decrease of the oscillations frequency is observed while decreasing V_{pg} . The divergence at $V_{\text{pg}} \approx -1.2$ V is an artefact arising from the rapid change of the mean resistance value at this plunger-gate voltage. **e,** Evolution of the resistance oscillations with both the plunger-gate voltage V_{pg} and the magnetic field variation δB after subtraction of a resistance background for each plunger-gate voltage sweep. Constant δR_{D} lines have a negative slope characteristic of oscillations induced by the Aharonov-Bohm effect.

XIV. ABSENCE OF CHARGING EFFECT

Here we discuss the absence of Coulomb blockade in graphene FP interferometers. We follow the approach proposed in ref.^{23,27} and estimate the relevant capacitances describing the electrostatics of the system. We use the notations of ref.²³, make approximate calculations for the small interferometer with a graphite back gate and discuss the case of the devices without graphite back gate. These calculations allow us to evaluate the parameter $\xi = \frac{C_{eb}}{C_b + C_{eb}}$, where C_b is the bulk-to-gate capacitance and C_{eb} the edge-to-bulk capacitance, which defines according to ref.²⁷ if the device is operating in the Aharonov-Bohm or Coulomb-dominated regime.

Bulk capacitance C_b

The bulk capacitance C_b refers to the capacitance of the electrons located in the central part of the cavity and spatially separated from the conducting edge channels. These bulk electrons belong to the last partially-occupied Landau level and form an isolated island capacitively coupled to the gate electrodes²⁶ (back gate, plunger gates, and split-gates). The electrostatic coupling of the bulk to the interfering edge channel is considered separately in another capacitance term C_{eb} discussed later.

For our device with a graphite back gate, the bulk capacitance is mostly given by $C_b = C_{bg}A_{geo}$ where $C_{bg} = 1.45 \text{ mF/m}^2$ is the effective back-gate capacitance and A_{geo} is the geometrical area. For our small FP cavity, we obtain $C_b = 4.5 \times 10^{-15} \text{ F}$. The corresponding bulk charging energy is thus $E_C = \frac{e^2}{2C_b} = 18 \text{ } \mu\text{eV}$ comparable to that reported for devices in GaAs heterostructures²⁴ in which AB oscillations with fractional edge channels were reported.

For our devices without graphite back gate, the 285 nm thick SiO_2 layer gives $C_{bg} = 0.12 \text{ mF/m}^2$. Thus for devices having similar sizes, C_b is approximately decreased by a factor 10 with respect to devices with graphite back gate. For the two devices presented in section XIII, BNGr64 and BNGr30, which respectively have geometrical surfaces of 11.5 and 10.1 μm^2 , we obtain respectively $C_b = 1.4$ and $1.2 \times 10^{-15} \text{ F}$.

On top of this bulk-to-back-gate capacitance, one needs to add the contribution of the plunger-gate and split-gate electrodes resting atop the 20 nm thick capping hBN. This contribution is difficult to evaluate because the top gates are not located directly above the bulk island. However, they still provide an additional parallel capacitive coupling leading to an increase of C_{bg} and a reduction of the overall bulk charging energy. We note that this effect may play a significant role in devices on silicon substrate and may become the main contribution to the bulk capacitance.

Interfering edge channel capacitance C_e

Similarly, the interfering edge channel is capacitively coupled to gates electrodes and one can define a edge-to-gates capacitance C_e . For a sake of completeness, we also evaluate it though it does not appear in the expression of ξ . C_e is the sum of two contributions : the edge-to-top-gates capacitance $C_{e/tg}$ and the edge-to-back-gate capacitance $C_{e/bg}$.

The latter can be evaluated following a similar approach as above. In this case, $C_{e/bg} = 2LwC_{bg}$ where $2L$ is the FP cavity perimeter and w is the width of the compressible stripe corresponding to the QH edge channel. Assuming $w = l_B$ the magnetic length ($\approx 7 \text{ nm}$ at 14 T), we obtain $C_{e/bg} = 8.6 \times 10^{-17} \text{ F}$. This contribution is likely to be increased by edge-channel reconstruction⁵⁹, which could occurs along the smooth potential of the pn-junctions.

On the other hand, $C_{e/tg} = C_{e/sg} + C_{e/pg}$ is the sum of the capacitance $C_{e/sg}$ between the split-gates and the interfering edge channel and the capacitance $C_{e/pg}$ between the plunger gate and the interfering edge channel. The latter can be extracted from the plunger-gate voltage period ΔV_{pg} of AB oscillations, as an oscillation corresponds to the addition/removal of one flux quantum inside the area enclosed by the edge channel and thus of an electron in the corresponding Landau level. Then, $C_{e/pg} = \frac{e}{\Delta V_{pg}} = 1.6 \times 10^{-17} \text{ F}$ for a typical voltage period $\Delta V_{pg} = 10 \text{ mV}$. Note that $C_{e/pg}$ scales as the perimeter L_{pg} of the plunger gate (geometrically 1.5 μm). From this evaluation, we can also estimate $C_{e/sg}$ by making the reasonable assumption that the electrostatics is the same for the split-gates and for the plunger gate. Thus $C_{e/sg} = \frac{L_{sg}}{L_{pg}} C_{e/pg} = 4.7 \times 10^{-17} \text{ F}$ with $L_{sg} = 4.4 \text{ } \mu\text{m}$ is the total length of the split-gate electrodes defining the cavity. The total edge capacitance is thus about $C_e = 1.5 \times 10^{-16} \text{ F}$.

In devices with silicon back gate, we expect C_e to be lower due to a smaller C_{bg} , but still of the same order of magnitude.

Edge-to-bulk capacitive coupling C_{eb}

The capacitive coupling between the edge and the bulk is the most difficult contribution to evaluate. We base our estimation on ref.⁶⁰, which proposes a model to describe the transport in a quantum dot in the QH regime composed of a conducting island enclosed and coupled to a conducting ring. Equation (19) in ref.⁶⁰ allows to evaluate C_{eb} based on the charge distribution induced by a potential difference between the interfering edge channel and the bulk compressible island separated by a distance a . For simplicity, we assume this distance to be of the order of l_B in graphene by analogy with GaAs heterostructures (see eq. (38) of ref.⁵⁹ giving the width of innermost incompressible stripe). The calculation of the capacitance also requires to set a characteristic length scale d over which the influence of the potential difference is screened by nearby gate electrodes. For our device with a graphite back-gate electrode, this length scale is imposed by the thickness of the bottom hBN such that $d \simeq 20$ nm. In these conditions, we can write:

$$C_{\text{eb}} = \frac{2L\epsilon_{\text{BN}}\epsilon_0}{2\pi^2} \ln\left(\frac{4d}{a}\right), \quad (1)$$

which leads to $C_{\text{eb}} = 2.8 \times 10^{-17}$ F.

We expect that C_{eb} remains of the same order of magnitude for devices with silicon back gate because the various top gates around the FP cavity are also 20 nm away from the graphene flake and, hence, set the cutoff length d . More specifically, for our devices BNGr64 and BNGr30, which respectively have perimeters $2L = 15.1$ and 13.3 μm , we obtain $C_{\text{eb}} = 5.0 \times 10^{-17}$ and 4.4×10^{-17} F. Alternatively, if we take $d = 285$ nm, we get $C_{\text{eb}} = 10.4 \times 10^{-17}$ and 9.1×10^{-17} F.

Discussion

From these calculations, we can estimate the parameter $\xi = \frac{C_{\text{eb}}}{C_{\text{b}} + C_{\text{eb}}}$. We obtain $\xi = 0.006$ for our 3.1 μm^2 device with graphite back gate, confirming that oscillations should arise from pure Aharonov-Bohm effect^{23,27}. Similarly, for our devices with silicon back gate, we obtain $\xi = 0.03 - 0.07 \ll 1$ also consistent with the observation of oscillations in the AB regime. This analysis is fully consistent with the absence of charging effect in our graphene devices.

XV. AHARONOV-BOHM OSCILLATIONS VERSUS DC VOLTAGE BIAS: ASYMMETRY AND DECAY

In this section, we discuss the oscillations induced by the application of a dc voltage bias and explain the origin of the tilted checkerboard pattern. We also analyze the decay of the oscillations amplitude with the voltage bias related to an energy relaxation or dephasing process.

Theoretical model for asymmetric potential drop

Here, we derive the formula for the transmission of a QH-FP interferometer as a function of magnetic field and voltage bias using the same formalism as in ref.⁴, but we take into account a possible asymmetric potential drop at the two QPCs.

The transmission of a non-interacting QH Fabry-Pérot interferometer reads:

$$t(\epsilon, \Phi) = \frac{t_1 t_2 e^{i\pi \frac{\Phi}{\Phi_0} + i \frac{L\epsilon}{\hbar v}}}{1 - r'_1 r_2 e^{2i\pi \frac{\Phi}{\Phi_0} + i \frac{2L\epsilon}{\hbar v}}}, \quad (2)$$

where $2\pi \frac{\Phi}{\Phi_0}$ is the Aharonov-Bohm phase, $\frac{2L\epsilon}{\hbar v}$ the dynamical phase accumulated by electrons after one winding in the cavity of length $2L$, t_1 and t_2 the transmission amplitudes of QPC₁ and QPC₂ for right moving particles, r'_1 the reflection amplitude for left-movers at QPC₁ and r_2 the reflection amplitude for right-movers at QPC₂.

The transmission probability is:

$$T(\epsilon, \Phi) = \frac{|t_1|^2 |t_2|^2}{1 + |r'_1 r_2|^2 - 2 |r'_1 r_2| \cos(2\pi \frac{\Phi}{\Phi_0} + \frac{2L\epsilon}{\hbar v} + \varphi)}, \quad (3)$$

where φ is a constant phase factor which depends on the scattering phase of the QPCs. Given that $|r_{1,2}|^2 = |r'_{1,2}|^2 = R_{1,2}$ and $|t_{1,2}|^2 = T_{1,2}$, we can rewrite (3) as

$$T(\epsilon, \Phi) = \frac{T_1 T_2}{1 + R_1 R_2 - 2\sqrt{R_1 R_2} \cos(2\pi \frac{\Phi}{\Phi_0} + \frac{2L\epsilon}{\hbar v} + \varphi)}. \quad (4)$$

In the weak backscattering limit, $R_i \ll 1$, and omitting the constant phase term φ , we obtain at first order:

$$T(\epsilon, \Phi) = 1 - R_1 - R_2 + 2\sqrt{R_1 R_2} \cos\left(2\pi \frac{\Phi}{\Phi_0} + \frac{2L\epsilon}{\hbar v}\right) \quad (5)$$

We then consider a finite dc voltage bias V applied between source and drain contacts. We note $q = -e < 0$ the electron charge. Depending on the energy relaxation processes consecutive to the current flow, and on the electrostatic coupling between the cavity, the back gate, the source and the drain, the electrochemical potential in the cavity will adjust itself at a value intermediate between that of the source and that of the drain. The right-movers coming from the source contact have an energy $qV^+ = qV(\frac{1}{2} + x) = qV\beta$ with respect to the chemical potential within FP cavity and the left-movers coming from the drain have an energy $qV^- = -qV(\frac{1}{2} - x) = -qV\bar{\beta}$. In these expressions, $x \in [-\frac{1}{2}, \frac{1}{2}]$ is the voltage bias asymmetry factor. $x = 0$ corresponds to a symmetric biasing with $V^+ = \frac{V}{2}$ and $V^- = -\frac{V}{2}$, meaning that the potential drop is the same across both QPCs. When $x = \frac{1}{2}$ (or equivalently $x = -\frac{1}{2}$) the bias is completely asymmetric, $V^+ = V$ and $V^- = 0$ (or equivalently $V^+ = 0$ and $V^- = -V$), the potential drop only occurs at one QPC while the FP cavity is at the same potential as one of the two contacts.

At zero temperature, the current through the device is given by $I = \frac{q}{h} \int_{qV^-}^{qV^+} T(\epsilon, \Phi) d\epsilon$. In the weak backscattering limit, it writes:

$$I = \frac{q}{h} \int_{qV^-}^{qV^+} \left[1 - R_1 - R_2 + 2\sqrt{R_1 R_2} \cos\left(2\pi \frac{\Phi}{\Phi_0} + \frac{2L\epsilon}{\hbar v}\right) \right] d\epsilon = I_0 + I_{\text{osc}}, \quad (6)$$

where $I_0 = \frac{e^2}{h} (1 - R_1 - R_2)V$ is the constant part of the current and I_{osc} is the oscillating part of the current which

writes:

$$I_{\text{osc}} = \frac{e^2}{h} 2\sqrt{R_1 R_2} \frac{\hbar v}{2Lq} \left[\sin\left(2\pi \frac{\Phi}{\Phi_0} + \frac{2L}{\hbar v} qV\beta\right) - \sin\left(2\pi \frac{\Phi}{\Phi_0} - \frac{2L}{\hbar v} qV\bar{\beta}\right) \right]. \quad (7)$$

The corresponding differential conductance is then:

$$\frac{dI_{\text{osc}}}{dV} = g_{\text{osc}} \left[\beta \cos\left(2\pi \frac{\Phi}{\Phi_0} - \frac{2L}{\hbar v} eV\beta\right) + \bar{\beta} \cos\left(2\pi \frac{\Phi}{\Phi_0} + \frac{2L}{\hbar v} eV\bar{\beta}\right) \right], \quad (8)$$

with $g_{\text{osc}} = \frac{e^2}{h} 2\sqrt{R_1 R_2}$ and restoring $q = -e$.

When the potential drop at the constrictions is symmetrical, that is, $V^+ = V/2$ and $V^- = -V/2$, we have $\beta = \bar{\beta} = \frac{1}{2}$ ($x = 0$) and then:

$$\frac{dI_{\text{osc}}}{dV} = g_{\text{osc}} \cos\left(2\pi \frac{\Phi}{\Phi_0}\right) \cos\left(2\pi \frac{L}{\hbar v} eV\right), \quad (9)$$

leading to a checkerboard pattern with a period versus bias voltage which is equal to the ballistic Thouless energy : $e\Delta V = \hbar v/L = E_{\text{Th}}$.

If the bias is completely asymmetrical, for example when $V^+ = V$ and $V^- = 0$ with $\beta = 1$ and $\bar{\beta} = 0$ ($x = \frac{1}{2}$), we obtain:

$$\frac{dI_{\text{osc}}}{dV} = g_{\text{osc}} \cos\left(2\pi \frac{\Phi}{\Phi_0} - 2\pi \frac{2L}{\hbar v} eV\right) \quad (10)$$

that draws a diagonal strip pattern with a period versus bias voltage (at fixed magnetic field) which is equal to half the Thouless energy. Any intermediate value of x leads to a mixed pattern, that is, a tilted checkerboard as observed in our experiment. Note that the measured diagonal resistance $\delta R_{\text{D}} = -\frac{dI_{\text{osc}}}{dV} \left(\frac{\hbar}{e^2}\right)^2$ shows exactly the same oscillatory features as the conductance in the weak backscattering limit.

In Fig. S18, we gather the results obtained in the three different interferometers as a function of voltage bias (Fig. S18a, c, d and f are respectively identical to Fig. 3c, d, e and f). The checkerboard patterns are tilted for our small (a) and medium interferometers (b), whereas the tilt is hardly visible for the largest interferometer (c). Using eq. (8), we can quantitatively reproduce in Fig. S18d, e and f the three experimental checkerboards with asymmetry parameters $x = 0.2$, 0.1 and 0.02 , respectively.

In our experiment, we apply a dc voltage to the source contact while the drain contact is kept grounded. The electrostatic coupling of the cavity to the back-gate electrode results in an asymmetric potential drop which could explain why the checkerboard patterns of our two smallest interferometers are tilted. On the other hand, the fact that the checkerboard pattern is nearly symmetric for the largest interferometer, indicates that energy relaxation processes equilibrate the chemical potential for sufficiently large interferometers, leading to a symmetric potential drop. Interestingly, tilted checkerboards in QH-FP interferometers has never been reported for GaAs QH-FP devices of the same size as our small interferometer, possibly due to the larger back-gate coupling in our graphene device equipped with a graphite back gate, or because the chemical potential equilibration is less effective in graphene.

Decay of the oscillations at finite bias

For an asymmetric potential drop characterized by an asymmetry factor x , the amplitude of the flux-periodic oscillations given by eq. (8) oscillates versus bias voltage with the following dependence:

$$\mathcal{A}(V, E_{\text{Th}}/e) = \sqrt{\cos^2\left(2\pi \frac{eV}{E_{\text{Th}}}\right) + 4x^2 \sin^2\left(2\pi \frac{eV}{E_{\text{Th}}}\right)} \quad (11)$$

Note that the period of this function is always the Thouless energy $E_{\text{Th}} = \hbar v/L$ whatever the asymmetry factor x , whereas the period of the conductance oscillations versus bias voltage at fixed magnetic field varies with the value of x (see for example eq. (9) and eq. (10)).

In Fig. S18a, b and c, however, we observe that the oscillations amplitude decays rapidly with the bias voltage and vanishes typically after one voltage period. Such a fast decay is much faster than the $1/\Delta V$ dependence predicted in ref.⁴ and was already reported by McClure and coworkers¹⁸ in GaAs QH-FP interferometers. These authors

found that an exponential decay of the oscillations amplitude with the bias describes correctly the data. Theoretical investigations²⁸ confirmed that Coulomb interactions can lead to an approximate exponential decay. Following this approach, we fitted the oscillations in our data with:

$$\mathcal{A}(V, \Delta V_{\text{expo}}) \exp\left(-2\pi\chi \frac{|V|}{\Delta V_{\text{expo}}}\right), \quad (12)$$

where χ is a phenomenological parameter that describes how fast the oscillations vanish with voltage, and ΔV_{expo} is the period of the resistance oscillations for this exponential decay. The amplitude of the oscillations is obtained by computing the Fourier amplitude of the resistance oscillations as a function of the plunger-gate voltage at fixed bias voltage. This leads to the lobe structure shown in Fig. S18g, h and i. A good agreement between the model and the data is found for the three interferometers. The extracted voltage periods ΔV_{expo} and damping factors χ are reported in Table III. It is worth noticing, however, that this phenomenological model does not capture the absence of secondary lobes in the experiments, suggesting that the decay of the oscillations is faster than exponential.

We therefore consider a second model with a Gaussian decay of the bias-induced oscillations. Investigations in Mach-Zehnder interferometers revealed that a Gaussian decay may arise from phase fluctuations of the interfering edge channel due to Coulomb interactions or the electric noise in the non-interfering edge channels^{49,61–63}. Within this approach, we fitted our data with:

$$\mathcal{A}(V, \Delta V_{\text{gauss}}) \exp\left(-\frac{V^2}{2V_0^2}\right), \quad (13)$$

where V_0 is the voltage scale characterizing the width of the Gaussian envelope, and ΔV_{gauss} the period of the resistance oscillation for this Gaussian decay. The fits of the experimental data with this expression are displayed in Fig. S18g, h and i (orange lines). This second model also describes well the data. The extracted voltage periods ΔV_{gauss} , reported in Table III, are close to those obtained with the exponential decay model. The extracted V_0 values scale linearly with the inverse interfering path length $1/L$ as mentioned in ref.⁴⁹ and is typically one third of ΔV_{gauss} .

The qualitative difference between the exponential and Gaussian decays is that the exponential decay fits better the amplitude of the first lobe but fails to reproduce the vanishing of the second ones, whereas the Gaussian model is less accurate for the first lobe but shows a suppressed second lobe.

QH-FP	ΔV_{expo} (μV)	χ	ΔV_{gauss} (μV)	V_0 (μV)
Small	134	0.42	128	40
Medium	83	0.42	81	25
Large	57	0.35	61	21

TABLE III. **Fitting parameters for the different models of bias-induced oscillation decay.** Voltage period ΔV_{expo} for the exponential decay model; χ damping rate for the exponential decay model; voltage period ΔV_{gauss} for the Gaussian decay model; V_0 width of the Gaussian envelope.

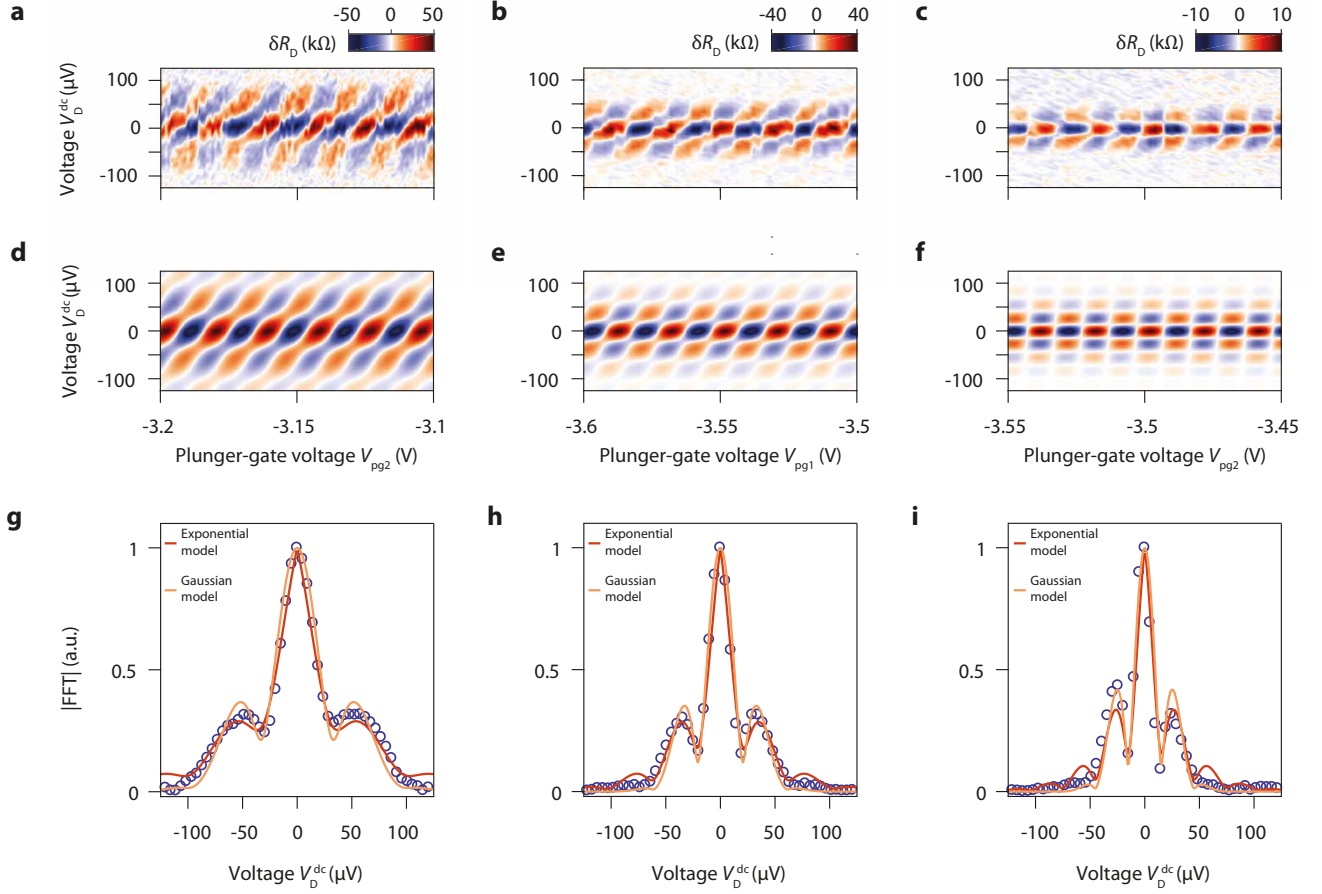


FIG. S18. **Bias dependence of Aharonov-Bohm oscillations.** **a, b, c**, Differential diagonal resistance variations δR_D , after background subtraction, versus dc diagonal voltage V_D^{dc} and plunger-gate voltage $V_{pg1,2}$ for the small, medium and large interferometer respectively in a, b and c. Interferences are obtained with the outer edge channel at 14 T. **e, f, g**, Numerical simulations of resistance oscillations induced by voltage bias and plunger-gate voltage that reproduce the data presented in a, b and c, respectively. The simulations incorporate an asymmetric potential drop at the two QPCs and an out-of-equilibrium decoherence factor. The voltage bias asymmetry factors of $x = 0.2$ and $x = 0.1$, respectively for the small d and medium interferometer e, are significant, indicating a limited chemical potential equilibration as opposed to the large interferometer f, which has a very small asymmetry term $x = 0.02$. **g, h, i**, Amplitude of the Fourier transform of the oscillations at fixed voltage bias (blue dots) and fits with eq. (12) (red line) and eq. (13) (orange line). Fitting parameters are reported in Table III.

XVI. TEMPERATURE DEPENDENCE OF THE AHARONOV-BOHM OSCILLATIONS: THERMAL AVERAGING

The effect of temperature on the visibility of the Aharonov-Bohm oscillations has been calculated in ref.⁴ in the limit of weak backscattering and at finite bias voltage for a symmetric potential drop at the two constrictions. This calculation considers only the thermal averaging of the interference and does not introduce decoherence by inelastic scattering or energy relaxation at finite bias.

Here we explain in details the calculation in the symmetric case and then extend the result to the case of an asymmetric potential drop as observed in our device. In the following, we use the expression of the transmission coefficient obtained in the previous section in the limit of weak backscattering:

$$T(E, \Phi) = 1 - R_1 - R_2 + \sqrt{R_1 R_2} \left(e^{i2\pi\Phi/\Phi_0} e^{iE2L/\hbar v} + e^{-i2\pi\Phi/\Phi_0} e^{-iE2L/\hbar v} \right) \quad (14)$$

Symmetric potential drop

Assuming a symmetric potential drop at the two constrictions as in ref.⁴, the current at finite temperature T and finite voltage V is given by:

$$I(\Phi, V, T) = \frac{q}{h} \int_{-\infty}^{+\infty} T(E, \Phi) \left(\frac{1}{1 + e^{(E - qV/2)/k_B T}} - \frac{1}{1 + e^{(E + qV/2)/k_B T}} \right) dE, \quad (15)$$

where $q < 0$ is the electron charge. Using the expression of the transmission coefficient in the limit of weak backscattering, the current writes:

$$I(\Phi, V, T) = \frac{q^2}{h} (1 - R_1 - R_2) V - \frac{q}{h} \sqrt{R_1 R_2} \left(e^{i2\pi\Phi/\Phi_0} H(V, T) + e^{-i2\pi\Phi/\Phi_0} H(V, T)^* \right), \quad (16)$$

where we introduce the function:

$$H(V, T) = \int_{-\infty}^{+\infty} e^{iE2L/\hbar v} \left(\frac{1}{1 + e^{(E - qV/2)/k_B T}} - \frac{1}{1 + e^{(E + qV/2)/k_B T}} \right) dE. \quad (17)$$

By changing the variable in the integral, it becomes:

$$H(V, T) = \left(e^{i\frac{qV}{2}2L/\hbar v} - e^{-i\frac{qV}{2}2L/\hbar v} \right) \int_{-\infty}^{+\infty} e^{iE2L/\hbar v} \frac{1}{1 + e^{E/k_B T}} dE, \quad (18)$$

where the choice of a symmetric potential drop influences only the term in the parenthesis. The calculation of the integral gives:

$$\int_{-\infty}^{+\infty} e^{iE2L/\hbar v} \frac{1}{1 + e^{E/k_B T}} dE = -i2\pi k_B T \sum_{n=0}^{+\infty} e^{-\omega_n 2L/\hbar v} = \frac{-i2\pi k_B T}{2 \sinh(\pi k_B T 2L/\hbar v)}, \quad (19)$$

where $\omega_n = (2n + 1)\pi k_B T$ are the Matsubara frequencies, with $n \in \mathbb{Z}$. In this case of a symmetric potential drop, the function $H(V, T)$ is real and writes:

$$H(V, T) = \sin(qVL/\hbar v) \frac{2\pi k_B T}{\sinh(\pi k_B T 2L/\hbar v)}. \quad (20)$$

The current finally writes:

$$I(\Phi, V, T) = G_0 V - \frac{q}{h} \sqrt{R_1 R_2} 2 \cos(2\pi\Phi/\Phi_0) \sin(qVL/\hbar v) \frac{2\pi k_B T}{\sinh(\pi k_B T 2L/\hbar v)}, \quad (21)$$

which is equivalent to equations (16) and (18) in ref.⁴. The differential conductance writes:

$$G(\Phi, V, T) = G_0 - \frac{q^2}{h} \sqrt{R_1 R_2} 2 \cos(2\pi\Phi/\Phi_0) \cos(qVL/\hbar v) \frac{\pi k_B T 2L/\hbar v}{\sinh(\pi k_B T 2L/\hbar v)}, \quad (22)$$

which forms a checkerboard pattern as a function of field and voltage. At high temperature, the visibility of these oscillations decreases exponentially with a dependence of the form:

$$e^{-\pi k_B T 2L/\hbar v} = e^{-4\pi^2 k_B T/E_{\text{Th}}} = e^{-T/T_0}, \quad (23)$$

where $E_{\text{Th}} = \hbar v/L$ is the ballistic Thouless energy which corresponds to the oscillation period $q\Delta V$ versus bias voltage, and T_0 is the fitting parameter of the exponential temperature dependence which is related to the Thouless energy by:

$$4\pi^2 k_B T_0 = E_{\text{Th}} = q\Delta V. \quad (24)$$

Asymmetric potential drop

In case of an asymmetric potential drop at the two constrictions (see section XV), the potential energy is $qV^+ = \beta qV$ at the source contact and $qV^- = -\bar{\beta}qV$ at the drain contact, with $\beta = \frac{1}{2} + x$ and $\bar{\beta} = \frac{1}{2} - x$ with the parameter $x \in [-\frac{1}{2}, \frac{1}{2}]$ characterizing the asymmetry of the potential drop. The current at finite temperature T and finite voltage V is then given by:

$$I(\Phi, V, T) = \frac{q}{h} \int_{-\infty}^{+\infty} T(E, \Phi) \left(\frac{1}{1 + e^{(E - \beta qV)/k_B T}} - \frac{1}{1 + e^{(E + \bar{\beta} qV)/k_B T}} \right) dE \quad (25)$$

Following the same calculations as above now gives the function:

$$H(V, T) = e^{ixqV2L/\hbar v} \sin(qVL/\hbar v) \frac{2\pi k_B T}{\sinh(\pi k_B T 2L/\hbar v)} \quad (26)$$

which contains a complex phase factor. The current writes:

$$I(\Phi, V, T) = G_0 V - \frac{q}{h} \sqrt{R_1 R_2} \ 2 \cos(2\pi\Phi/\Phi_0 + xqV2L/\hbar v) \sin(qVL/\hbar v) \frac{2\pi k_B T}{\sinh(\pi k_B T 2L/\hbar v)} \quad (27)$$

which is modified only by the term $xqV2L/\hbar v$ in the cosine function. The differential conductance writes:

$$G(\Phi, V, T) = G_0 - \frac{q^2}{h} \sqrt{R_1 R_2} \ 2g(\Phi, V) \frac{\pi k_B T 2L/\hbar v}{\sinh(\pi k_B T 2L/\hbar v)} \quad (28)$$

where the oscillation term:

$$g(\Phi, V) = \cos(2\pi\Phi/\Phi_0 + xqV2L/\hbar v) \cos(qVL/\hbar v) - 2x \sin(2\pi\Phi/\Phi_0 + xqV2L/\hbar v) \sin(qVL/\hbar v) \quad (29)$$

gives a titled checkerboard pattern as a function of field and voltage for $x \neq 0$. It is interesting to note that the temperature dependence is not affected by the asymmetry of the potential drop at the constrictions. The fitting parameter T_0 of the exponential temperature dependence is still related to the ballistic Thouless energy by $4\pi^2 k_B T_0 = E_{\text{Th}}$.

XVII. EVALUATION OF THE PHASE COHERENCE LENGTH L_ϕ

To estimate the phase coherence length L_ϕ in our graphene QH-FP interferometers, we assume that the visibility \mathcal{V} of coherent oscillations scales as:

$$\mathcal{V} = \mathcal{V}_0 \frac{2L/L_T}{\sinh(2L/L_T)} \exp\left(-\frac{2L}{L_\phi(T)}\right) \quad (30)$$

where $L_T = \frac{hv}{2\pi^2 k_B T}$ is the characteristic length associated with the decay of the visibility due to thermal averaging at temperature T (see eq. (22) in previous section), $L_\phi(T)$ is the phase coherence length that can depend on temperature, $2L$ is the the perimeter of the FP cavity and \mathcal{V}_0 is the asymptotic limit reached by the visibility when L tends to zero. Note that the exponential decrease due the finite coherence length is only valid for $2L$ above L_ϕ and should saturate to a particular visibility below unity for smaller perimeters.

Fitting the evolution of \mathcal{V} with $2L$ at fixed temperature with eq. (30) provides a direct estimate of L_ϕ . As visibility depends on the QPC transmissions, we performed this length-dependence analysis by considering our best visibility data obtained for the three sizes of interferometers at 14 T. We evaluate the electron temperature at our base fridge temperature to be $T \simeq 20$ mK, which corresponds to the temperature below which the T -dependence of the visibility saturates. For experiments with the inner edge channel, we extracted the visibility through $\frac{G_{\max} - G_{\min}}{(G_{\max} - e^2/h) + (G_{\min} - e^2/h)}$, which subtracts the conductance contribution of the fully transmitted outer edge channel.

Fig. S19 shows the evolution of these visibilities \mathcal{V} with the perimeter of the interferometers $2L$. For comparison, the decrease of the visibility induced by the thermal broadening at 20 mK is also shown with the solid red line (eq. (30) with $L_\phi(T)$ infinite and a edge state velocity of 1.4×10^5 m/s, giving $L_T = 17 \mu\text{m}$). For both experiments with the outer and the inner edge channel, a fast decrease of \mathcal{V} with $2L$ is observed which cannot be explained by the effect of thermal broadening. The best visibilities for both interfering edge channels are virtually the same except for data in the large interferometer with the inner edge channel, which shows a significant drop compared to the data with the outer one. It probably reflects that the tuning of the QPC could have been improved. We thus discard it for our quantitative analysis.

By fitting the visibility decay, we extract a phase coherence length $L_\phi \approx 10 \mu\text{m}$ at 20 mK and 14 T. The obtained value of $10 \mu\text{m}$ is smaller or comparable to the perimeter length, which justifies the exponential decrease used in eq. (30) (the saturation would appear for smaller perimeters as the ones studied here). This value is also consistent with the observation of coherent Aharonov-Bohm oscillations in the double FP cavity at base temperature.

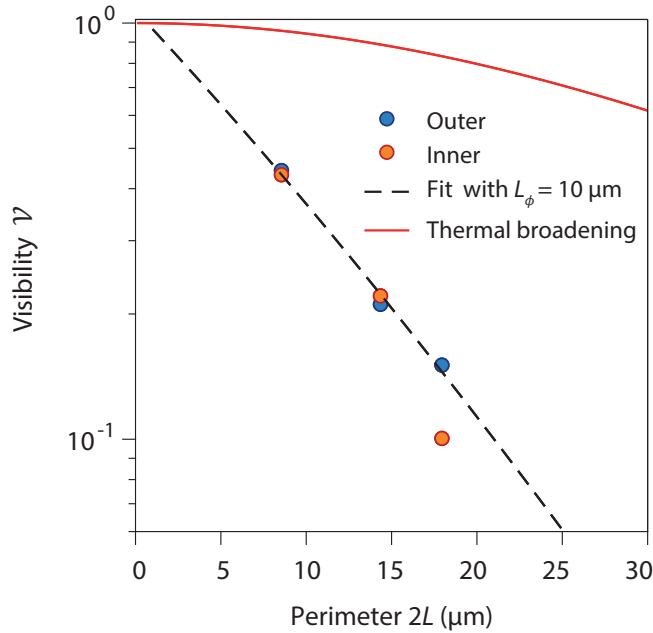


FIG. S19. **Phase coherence length L_ϕ .** Evolution of the best visibilities \mathcal{V} with the perimeter $2L$ of the interferometers obtained in experiments at base temperature with the outer (blue dots) and the inner (red dots) edge channel. The red solid line shows the thermal broadening contribution. The fit of the data (black dashed line) with eq. (30) and discarding the inner edge channel experiment for the large interferometer, provides a coherence length of $10 \mu\text{m}$ at 20 mK.

XVIII. ANALYSIS OF THE DOUBLE-CAVITY INTERFEROMETER

In this section we discuss the experiments performed in the coherently-coupled double FP cavity. We first derive the theoretical expression for the transmission for a double cavity and then compare it with our data to show that electron transport remains coherent in the overall device.

The transmission and reflection amplitudes of a Fabry-Pérot interferometer reads:

$$t_{\text{FP}}(\varphi) = \frac{t_1 t_2 e^{i\varphi}}{1 - r'_1 r_2 e^{i2\varphi}}, \quad (31)$$

$$t'_{\text{FP}}(\varphi) = \frac{t'_1 t'_2 e^{i\varphi}}{1 - r'_1 r_2 e^{i2\varphi}}, \quad (32)$$

$$r_{\text{FP}}(\varphi) = r_1 + \frac{r_2 t_1 t'_1 e^{i2\varphi}}{1 - r'_1 r_2 e^{i2\varphi}}, \quad (33)$$

$$r'_{\text{FP}}(\varphi) = r'_2 + \frac{r'_1 t_2 t_2 e^{i2\varphi}}{1 - r'_1 r_2 e^{i2\varphi}}, \quad (34)$$

where 2φ is the Aharonov-Bohm phase accumulated by electrons after one winding in the cavity, t_i (t'_i) the transmission amplitude, and r_i (r'_i) the reflection amplitude of QPC $_i$ for right (left) moving particles.

The total transmission amplitude t_{tot} of two coupled FP cavities can be calculated using the transmission and reflection amplitudes of one FP cavity and the transmission and reflection amplitudes of a third QPC. Thus, using the previous expressions, we have:

$$t_{\text{tot}}(\varphi_1, \varphi_2) = \frac{t_{\text{FP}}(\varphi_1) t_3 e^{i\varphi_2}}{1 - r'_{\text{FP}}(\varphi_1) r_3 e^{i2\varphi_2}}, \quad (35)$$

where $2\varphi_1$ and $2\varphi_2$ are the Aharonov-Bohm phase accumulated by electrons after one winding in the cavity between QPC $_1$ and QPC $_2$ and between QPC $_2$ and QPC $_3$, respectively.

Using $|t_i|^2 = |t'_i|^2 = T_i$, $|r_i|^2 = |r'_i|^2 = R_i$ and the relation $r'_i = -\bar{r}_i t'_i / \bar{t}_i$ (the overline indicates complex conjugate), we can express the transmission as:

$$T_{\text{tot}}(\phi_1, \phi_2) = \frac{T_1 T_2 T_3}{|1 - \sqrt{R_1 R_2} e^{i\phi_1} - \sqrt{R_2 R_3} e^{i\phi_2} + \sqrt{R_1 R_3} e^{i(\phi_1 + \phi_2)}|^2} = \frac{T_1 T_2 T_3}{D}, \quad (36)$$

where ϕ_1 and ϕ_2 are the Aharonov-Bohm phases acquired when quasiparticles wind into the medium and small cavities respectively (including the phase factor from the reflection amplitudes of the QPCs). The denominator D can be written as:

$$D = 1 + R_1 R_2 + R_3 R_2 + R_1 R_3 - 2(1 + R_3) \sqrt{R_1 R_2} \cos(\phi_1) - 2(1 + R_1) \sqrt{R_2 R_3} \cos(\phi_2) + 2\sqrt{R_1 R_3} \cos(\phi_1 + \phi_2) + 2R_2 \sqrt{R_1 R_3} \cos(\phi_1 - \phi_2). \quad (37)$$

In this expression, four oscillation frequencies emerge, namely, ϕ_1 , ϕ_2 , $\phi_3 = \phi_1 + \phi_2$ and $\phi_4 = \phi_1 - \phi_2$. The terms in ϕ_3 and ϕ_4 in eq. (37), which result from coherent interferences through the two interferometers, does not have the same prefactor : the amplitude of the ϕ_3 oscillations is larger than the amplitude of the ϕ_4 oscillations which is even negligible in the weak backscattering limit. In contrast, in a situation where the transport through the double cavity would be incoherent, one could expect the appearance of term in the form of $\cos(\phi_1) \times \cos(\phi_2) = \frac{1}{2} [\cos(\phi_3) + \cos(\phi_4)]$ which would lead to equal amplitudes of ϕ_3 and ϕ_4 oscillating components.

Relating this model to our device geometry, we can ascribe to each of these four Aharonov-Bohm phases a coupling to the relevant plunger gates:

$$\phi_1 \simeq \frac{2\pi}{\Phi_0} (\delta A_1 B + A_1 \delta B) = \frac{2\pi}{\Phi_0} (\alpha_1 V_{\text{Pg}1} B + A_1 \delta B), \quad (38)$$

$$\phi_2 \simeq \frac{2\pi}{\Phi_0}(\delta A_2 B + A_2 \delta B) = \frac{2\pi}{\Phi_0}(\alpha_2 V_{pg2} B + A_2 \delta B), \quad (39)$$

$$\phi_3 \simeq \frac{2\pi}{\Phi_0}[(\delta A_1 + \delta A_2)B + (A_1 + A_2)\delta B] = \frac{2\pi}{\Phi_0}[(\alpha_1 V_{pg1} + \alpha_2 V_{pg2})B + (A_1 + A_2)\delta B], \quad (40)$$

$$\phi_4 \simeq \frac{2\pi}{\Phi_0}[(\delta A_1 - \delta A_2)B + (A_1 - A_2)\delta B] = \frac{2\pi}{\Phi_0}[(\alpha_1 V_{pg1} - \alpha_2 V_{pg2})B + (A_1 - A_2)\delta B], \quad (41)$$

where A_1 and A_2 are the area of the medium and small cavities, respectively, V_{pg1} and V_{pg2} the plunger-gate voltages that tune these areas and α_1 and α_2 their lever arms.

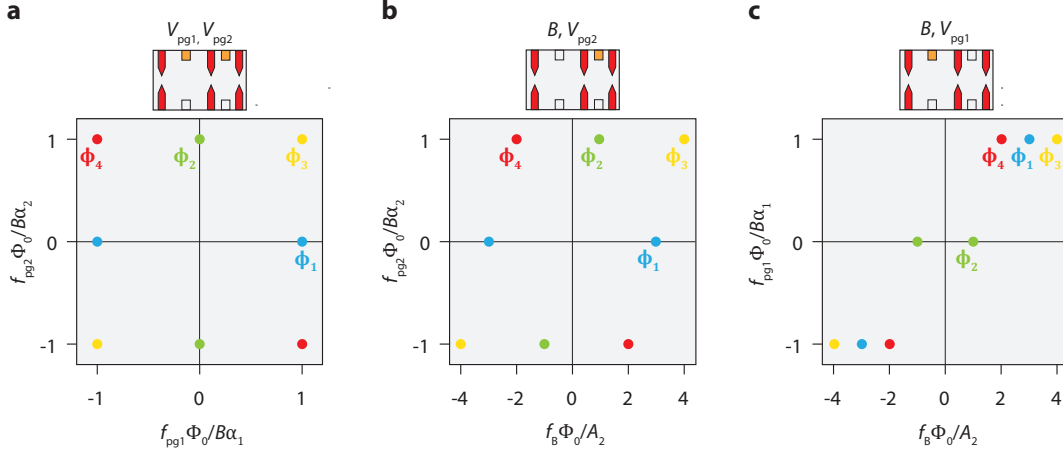


FIG. S20. **Fourier analysis of double QH-FP interferometer.** **a, b, c,** Positions in reciprocal space of the oscillation frequencies for three different configurations of interferometry experiments (assuming $A_1 = 3A_2$). Each peak is labelled with its Aharonov-Bohm phase. Top schematics depict the active QPCs (red) and plunger gates (orange) in each experiments. The parameters used to tune the Aharonov-Bohm phases in each case are indicated above the corresponding schematic.

In Figure S20 we show the expected frequencies in Fourier space for a coherently-coupled double QH-FP interferometer upon varying both plunger gates (Fig. S20a), or one plunger gate and the magnetic field (Fig. S20b and c). For the former case, the plunger-gate frequencies corresponding to the small and medium interferometers are located on the x and y axis, reflecting the terms ϕ_1 and ϕ_2 in eq. (37), whereas the double interferometer terms ϕ_3 and ϕ_4 that depend on both plunger gates are located on the diagonals. For latter configurations, the frequency of the interferometer without the active plunger gate depends only on B and is thus located at zero plunger-gate frequency on the horizontal axis (ϕ_1 in b and ϕ_2 in c), whereas the frequency of the other interferometer with the active plunger gate, as well as the coupled interferometer frequencies, are located at finite plunger gate frequency.

In Figure S21 we reproduce the data shown in Fig. 4 for the coherently-coupled QH-FP interferometer and add the configuration with V_{pg1} active and magnetic field (Fig. S21c), which provides another confirmation of the presence of the ϕ_3 contribution. The four quadrants of the Fourier amplitudes are shown in order to check the presence of the $\phi_4 = \phi_1 - \phi_2$ frequency. The ϕ_4 frequency, whose expected location is indicated by the red circle in Fig. S21d-f, is clearly present in the configuration of Fig. S21e. Its amplitude is smaller than the amplitude of the ϕ_3 contribution as expected in eq. (37). For the two other configurations, this ϕ_4 frequency is hardly visible. This detailed analysis provides compelling evidence for coherent transport through the three QPCs.

We can furthermore simulate the data by a simplified model that neglects terms in R^2 in eq. (37):

$$\delta R = \delta R_1 \cos(\phi_1) + \delta R_2 \cos(\phi_2) + \delta R_3 \cos(\phi_3). \quad (42)$$

Using the experimental Fourier amplitudes for the parameters δR_1 , δR_2 and δR_3 we obtain the resistance maps shown in Fig. S21g-i that reproduce the experimental maps in Fig. S21a-c with excellent fidelity.

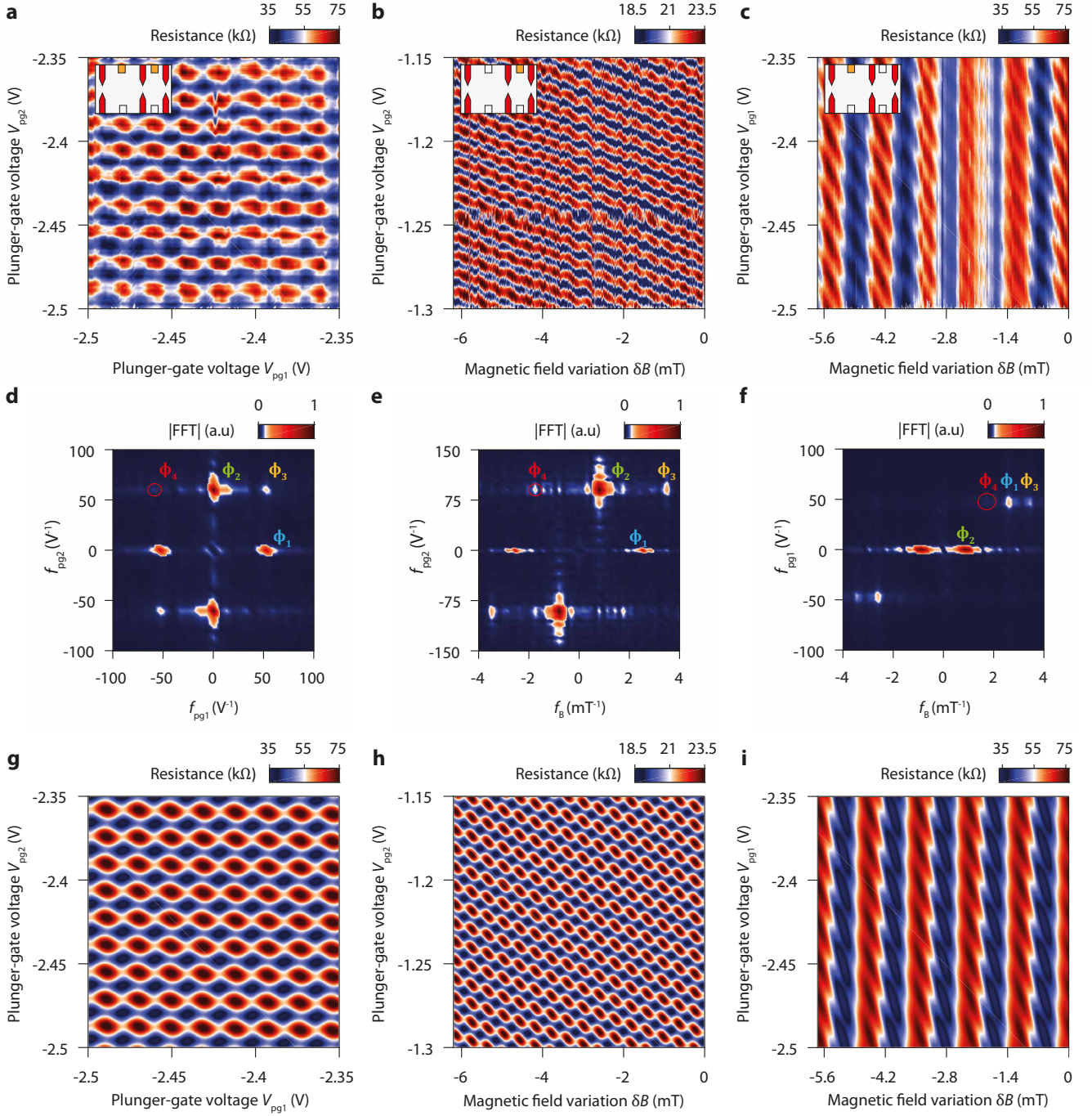


FIG. S21. **Coherently-coupled double QH-FP interferometer.** **a**, Diagonal resistance versus plunger-gate voltages V_{pg1} and V_{pg2} (outer edge channel interfering, $B = 14$ T). **b**, Diagonal resistance versus magnetic field variation δB and plunger-gate voltage V_{pg2} (inner edge channel interfering, $B = 14$ T). **c**, Diagonal resistance versus magnetic field variation δB and plunger-gate voltage V_{pg1} (outer edge channel interfering, $B = 14$ T). The inset schematics in **a**, **b** and **c** indicate the active QPCs (in red) and plunger gates (in orange) for the respective measurements. **a** and **b** are identical to the Fig. 4c and 4d of the main text. **d**, **e**, **f**, Four-quadrant Fourier amplitude of the resistance oscillations displayed respectively in **a**, **b** and **c** in their respective reciprocal space. The peaks corresponding to the different Aharonov-Bohm phases are identified in each case. **g**, **h**, **i**, Numerical simulations reproducing the experiments shown respectively in **a**, **b** and **c** with eq. (42). The parameters $(\delta R_1, \delta R_2, \delta R_3)$ are $(0.66, 1, 0.18)$ in **g**, $(0.64, 1, 0.22)$ in **h**, and $(0.19, 1, 0.11)$ in **i**.